HHS Public Access

Author manuscript

Nat Cell Biol. Author manuscript; available in PMC 2026 September 02.

Published in final edited form as:

Nat Cell Biol. 2026 September ; 28(9): 1799–1813. doi:10.1038/s41556-026-02052-1.

Elevated contractility drives age-associated implantation failure in mouse embryos from aged females

Kate E. Cavanaugh[1,2], **MJ Franco-Oñate**[3,4], **Nicole Horsley**[5,6], **Dilan Gokyer**[7], **Tomiris Atazhanova**[7], **Diana J. Laird**[8], **Patrick W. Oakes**[9], **Joan K. Riley**[7], **Francesca E. Duncan**[7], **MaryEllen Pavone**[7], **Matteo Molé**[5,6,10], **Ricard Alert**[3,4,11,12,13,14], **Orion D. Weiner**[1,2]

[1]Cardiovascular Research Institute, University of California, San Francisco, San Francisco, CA, USA

[2]Department of Biochemistry and Biophysics, University of California, San Francisco, San Francisco, CA, USA

[3]Max Planck Institute for the Physics of Complex Systems, Dresden, Germany

[4]Center for Systems Biology Dresden, Dresden, Germany

[5]Division of Reproductive, Stem Cell and Perinatal Biology, Department of Obstetrics and Gynecology, Stanford University School of Medicine, Stanford, CA USA

[6]Institute for Stem Cell Biology and Regenerative Medicine, Stanford, CA USA

[7]Department of Obstetrics and Gynecology, Feinberg School of Medicine, Northwestern University, Chicago, IL, USA

[8]Department of Obstetrics, Gynecology, and Reproductive Sciences, University of California, San Francisco, San Francisco, CA, USA

[9]Department of Cell and Molecular Physiology, Loyola University Chicago Stritch School of Medicine, Chicago, IL USA

[10]Dunlevie Maternal Fetal Medicine Center for Discovery, Innovation and Impact, Stanford University School of Medicine, Stanford, CA USA

[11]Cluster of Excellence Physics of Life, TU Dresden, Dresden, Germany

[12]Departament de Física de la Matèria Condensada, Universitat de Barcelona, Barcelona, Spain

[13]Universitat de Barcelona Institute of Complex Systems (UBICS), Barcelona, Spain

[14]Institució Catalana de Recerca i Estudis Avançats (ICREA), Barcelona, Spain

Abstract

Corresponding author: Orion Weiner, Orion.Weiner@ucsf.edu.

Author Contributions KEC, ODW, and DJL conceived of the study. KEC collected and analyzed data. MJFO and RA developed the theory and fitted it to the data. PWO assisted with optimization and analysis of TFM experiments. KEC, ODW, MJFO, and RA wrote the original draft. DG, TA, JKR, FED, MEP obtained and extracted all Embryoscope data. KEC analyzed the Embryoscope data. NH and MM contributed to the human blastocyst thawing and staining. All authors edited the manuscript. All authors approved the final version of the article.

Competing Interests Statement: The authors declare no competing interests.

Women in their mid-thirties experience a marked decline in fertility. The origin of these fertility defects resides in the implantation capacity of the embryo itself, but the mechanistic basis of this impairment is not well-understood. Here, we identify a core mechanical defect in embryos from aged females that impairs their implantation competence. Using mouse models, we find that reproductive aging drives excessive contractility in the trophectoderm, the outer epithelial lineage that enables implantation. This hypercontractility increases blastocyst tissue surface tension and viscosity, which hinders spreading during implantation. Elevated contractility is both necessary and sufficient for age-associated implantation failure. We identify non-invasive imaging signatures that infer embryo mechanics and predict implantation success for embryos of both young and aged females. Analyses of human embryos and IVF clinical datasets reveal conserved age-associated mechanical alterations that correlate with implantation potential. Our work implicates embryo mechanics as a key regulator of reproductive longevity.

Introduction

Female fertility sharply declines as a woman's reproductive organs rapidly age after 35 years, sometimes decades before any other organ system or that of her male counterparts. For women over the age of 35, the probability of achieving a full-term pregnancy per cycle declines to approximately 15% and decreases sharply with advancing age, with over 60% of miscarriages occurring around the time of embryo implantation[1–4]. Age-related infertility was originally attributed to the uterine microenvironment, in which the endometrium was thought to become increasingly stiff, fibrotic, and less receptive to implantation[5,6]. However, clinical outcomes from In Vitro Fertilization (IVF) challenge this view, as pregnancy rates in older women are largely rescued when using donor eggs from younger women[7]. These IVF data suggest that the egg and not the uterus is the dominant driver of age-associated infertility. While the reproductive aging field has historically focused on age-associated loss of egg quality, few studies have assessed age-related changes to embryo morphogenesis post-fertilization through the critical failure point of implantation. These peri-implantation stages are fundamentally biophysical, encompassing embryo-uterine adhesion and mechanically-driven invasion that facilitate postimplantation morphogenesis. Age-related changes in embryo mechanics may compromise an embryo's ability to undergo the complex morphogenetic events required for successful uterine integration[8–13], but the underlying embryonic defects remain poorly understood. Because the average age of maternal childbirth continues to rise worldwide, uncovering how maternal aging impacts the earliest stages of embryo development represents a pressing, unresolved challenge with significant implications for both basic biology and the optimization of IVF outcomes.

A major barrier in the IVF field lies in selecting blastocysts that will successfully lead to a full-term pregnancy[14–17]. Despite decades of refinement, current screening approaches yield only about a 40% success rate for younger women and a 15% success rate for women over the age of 35[18,19]. The gold-standard assessment of embryo quality remains the gross morphology of the blastocyst structure[20,21]. Here, IVF grading typically evaluates how effectively the primitive placental trophectoderm (TE) epithelial layer encloses the fluid-filled cavity surrounding the compact, fetal Inner Cell Mass (ICM) (Fig. 1a). However,

morphological grading is subjective, context-dependent, and does not always predict embryo viability. More recently, additional screening methods have included the biopsy of Trophectoderm cells for aneuploidy testing[22,23]. Although chromosomal abnormalities are prevalent in human embryos, many embryos labeled “euploid” still exhibit implantation defects[23]. This highlights that chromosomal status, while important, does not fully capture the developmental competence of an embryo. Together, these limitations underscore a critical gap: neither general morphology nor genetic screening reliably captures the functional viability of an embryo.

Here, we investigate the developmental origins of age-related infertility by combining approaches from classical mammalian embryology, developmental cell biology, and biophysics. By applying engineering and biophysical approaches to reproductive health, our work reveals a mechanical origin of age-related implantation defects: hyperactive contractility in mouse embryos from older females impairs multiple developmental events, including cell fate specfication and uterine implantation. Mouse models replicate age-related defects seen in humans, as assessed by pregnancy outcomes and *in vitro* implantation assays. Here, advanced maternal age is associated with slow Trophectoderm spreading on synthetic gel substrates. Heightened embryo contractility is both necessary and sufficient for the age-related implantation defects. This peri-implantation defect can be explained by increased surface tension, substrate adhesion, and viscosity of the embryo, which oppose spreading during implantation in a similar manner that increased viscosity impairs the wetting of a droplet on a 2D surface. We find that early mechanical defects originate at the 8-cell stage and alter both YAP signaling and lineage specification. Our experiments link aberrant mechanics to reduced trophectoderm potential at implantation. We further identify non-invasive imaging signatures that infer embryo mechanics and predict implantation success for mouse embryos of both young and aged females. Analyses of human embryos and IVF clinical datasets reveal conserved age-associated mechanical alterations that correlate with implantation potential. Our work implicates embryo mechanics as a key regulator of reproductive longevity and provides a potential foundation for rationally screening embryos to improve IVF outcomes.

Results

Mouse models replicate human age-associated implantation defects

A decline in human age-associated fertility can be observed in public datasets of IVF blastocyst-uterine transfers (Fig. 1b)[24]. This Assisted Reproductive Technology sought to improve fertility outcomes through the collection of eggs from gonadotropin-stimulated donor females following fertilization and transfer to the uterus of a surrogate mother. When donor embryos were collected from younger women (less than 35 years of age) and transferred to similarly young surrogates, a 30% live birth rate was achieved in this IVF procedure. When embryos were collected from older females (beyond 35 years of age) and transferred to older surrogates, the live birth rate dropped to 18%, recapitulating the sharp decline in female fertility as women’s reproductive organs rapidly age after 35 years. Older surrogates receiving embryos from younger female donors exhibited a rescue of fertility to 30% live birth rate, indicating that an older woman’s uterus is receptive to embryo

implantation. These data suggest that the origin of maternal age-associated infertility is the egg or early embryo, but the basis of this defect is not known.

We leveraged the mouse as a model to investigate the embryonic origin of age-related infertility with a focus on implantation, the stage at which most pregnancy failures occur in humans. The early mouse embryo is amenable to *ex utero* culture, concurrent long-term quantitative microscopy, genetic manipulation by microinjection or electroporation, live-imaging using cell-permeable dyes to visualize protein localization, and mRNA-encoded fluorescent protein expression[25–30]. Murine lineage specification and early preimplantation morphogenetic checkpoints are also analogous to human embryogenesis[31]. Furthermore, the mouse embryo undergoes implantation through similar mechanisms to humans, albeit with notable differences in post-implantation morphogenesis (Fig. 1a)[32–35].

To test the effects of maternal age on pregnancy outcome in mice while modeling the clinical practice used in humans, we leveraged the well-established technique of Non-Surgical Embryo Transfer (NSET)[25,36]. Non-invasive insertion of experimental blastocysts into the uterine horn of a pseudopregnant female by NSET enabled subsequent implantation and full-term pregnancy, after which litter sizes were tracked. This scheme enabled us to quantify live birth rates similar to published IVF datasets (Fig. 1b). In this experimental workflow, we used young sexually mature male mice (<35 weeks of age) to remove the variable of paternal age. We bred males to females from two distinct age groups: young (6-9 weeks old) and aged (40+ weeks old), roughly equivalent to women in their 20's and 40's, respectively[37,38] (Fig. 1c). Embryos pooled from younger female donors (which we termed as "young embryos") were cultured to blastocyst stage and transferred to young surrogate females, which resulted in a 39% live birth rate. Embryos from older female donors (which we termed as "aged embryos") transferred to aged surrogates, resulted in an 14% success rate, recapitulating the age-related decline in fertility seen in humans. Like their human counterparts, aged mice were rescued to a fertility rate of 38% when they were recipients of young embryos, consistent with an embryonic origin of age-related infertility in both mice and humans. We subsequently focused on a more experimentally tractable system to probe the effect of maternal age on embryo implantation.

The biophysical mechanisms underlying implantation mediated by the trophectoderm remain largely unexplored due to technical limitations of visualizing *in utero* processes. We overcame this barrier by combining biomechanical measurements with previously-established and highly efficient *in vitro* implantation assays[39,40]. This *ex utero* platform harnesses synthetic collagen-coated polyacrylamide (PAA) gels and specialized IVC media to mimic the physiochemical nature of the receptive maternal tissue during embryo-substrate attachment and spreading. Extending *ex vivo* implantation to mouse embryos, we achieved over 90% attachment rates of embryos to the gel substrate, similar to previous reports (ED. Fig. 1a)[39,40].

To visualize spreading dynamics during trophectoderm invasion in our *in vitro* assays, we performed live confocal microscopy of E4.5 blastocysts stained with 650-FastAct for 24 hours post-implantation[25]. To limit phototoxicity over this extended period, we limited our imaging to the future implantation site at the mural Trophectoderm (mTE) region of the

blastocyst to capture its attachment and outgrowth 24-hours post-adhesion (Fig. 1d, Supp. Movie 1). We defined the initiation of implantation (t_0=0hrs) as the transition between a coherent trophectoderm epithelia and the appearance of protrusive trophectoderm cells at the basal substrate (Fig. 1d **inlays**). By imaging actin dynamics every 15 minutes over 24 hours, we captured the dynamics of implantation, including initial blastocyst-substrate attachment, cavity collapse, and full trophectoderm outgrowth (Figs. 1d, Supp. Movie 1). Embryos from young mothers displayed efficient spreading dynamics, characterized by a relatively rapid transition between attachment, spreading, and outgrowth (ED. Fig. 1b). While maternally aged embryos initially attached to the substrate, their spreading resulted in a significant reduction in the final trophectoderm contact area at 24 hours post attachment (Fig. 1e). These data indicate a dampening of implantation potential that arises with advanced maternal age.

Enhanced contractility is necessary and sufficient for maternal age-related implantation defects

What is the origin of reduced trophectoderm implantation in embryos from aged mothers? Cellular contractility is known to be a primary regulator of tissue spreading in other contexts, including the invasion of cancer aggregates[41,42]. Mouse embryos exert contractile pulling forces at cell-substrate adhesions to mediate outward spreading of the trophectoderm during implantation[32]. Here, contractility acts to increase cell-substrate interactions to promote spreading. However, contractility can also act in cell-cell adhesion to limit tissue spreading. As such, it is not a priori clear whether increasing contractility should promote or hinder tissue spreading. We therefore probed whether alterations in contractility underlie the defective spreading in embryos from aged females. To investigate whether blastocyst contractility plays a functional role in embryo implantation, we used pharmacological regulators of actomyosin-based contractility (Figs. 2a).

We first harnessed the cell-permeable RhoA-activator CN03 (Figs. 2a). RhoA is a master regulator of contractility that functions by activating actin polymerization and myosin-mediated contractile force generation. CN03 potentiates RhoA activity by inhibiting GAP-associated GTP hydrolysis to increase the level of GTP-bound RhoA within 2-4 hours[43]. We added CN03 to embryo culture medium starting at the 2-cell stage and then assessed the effects on implantation potential. Gel-implanted embryos were fixed at 30hrs post-implantation to ensure adhesion of experimental blastocysts and proper spreading as observed in our live-imaging (Figs. 1d–e). Young embryos treated with ectopic RhoA activator CN03 displayed a striking reduction in spread area analogous to maternally aged embryos (Fig. 2b).

Enhanced contractility was sufficient to impair trophectoderm spreading in embryos from younger females, mimicking the defects observed in embryos from older mothers. To probe whether enhanced contractility is required for the maternal age-related defect in implantation, we attempted to rescue trophectoderm spreading by reducing contractility in aged embryos (Figs. 2a). We cultured maternally aged embryos in the FDA-approved Y-compound derivative, Ripasudil, which modulates myosin-mediated contractility through inhibiting the activity of Rho-Kinase, ROCK[44,45]. Ripasudil-treated maternally aged

embryos exhibited rescued spread area in our *in vitro* implantation assays, indicating a necessary role for actomyosin contractility in the spreading defects in aged embryos (Fig. 2c).

We finally confirmed blastocyst contractility as a function of advanced maternal age by immunostaining E4.5 blastocysts with the tension sensor, VD7, which recognizes cell-cell junctions under strain[46] (ED. Fig. 2a). The mural Trophectoderm region in the aged condition exhibited significant increases in normalized junctional VD7, consistent with increased tissue tension in the site of future implantation. Maternally aged embryos also exhibited increased normalized junctional Non-Muscle Myosin isoform IIb (MYH10) and phosphorylated Myosin Light Chain (pMLC) (ED. Figs. 2b–c), both indicators of increased tissue tension and heightened contractility.

Because increased contractility in embryos from older females was necessary and sufficient for the observed spreading defects, this indicates a causative role for contractility in dampening embryo implantation mechanics. Our data suggest an optimal regime of contractility for cell spreading. While a certain level of contractility is necessary for outward tissue migration, further increases in contractility (through aging or pharmacological manipulation) hinder embryonic implantation.

Advanced maternal age impairs blastocyst wetting

We next turned to physical models of tissue spreading to better understand how enhanced blastocyst contractility produces age-related implantation defects. Based on previous work[33,41,48], we describe implantation using active wetting theory, which models the 3D blastocyst structure as an active liquid droplet spreading on a 2D surface, such as the uterine lining (Fig. 3a). Active wetting theory predicts that tissue spreading depends on the competition between blastocyst surface tension and exerted cell-substrate forces. These two forces can have opposite effects; surface tension of the blastocyst acts to minimize contact with the substrate, while cell-substrate forces promote blastocyst spreading (Fig. 3b).

We hypothesized that the defective spreading of blastocysts in the aged condition could arise from changes in mechanical forces during the preimplantation period. To test this hypothesis, we performed direct mechanical measurements of late E4.5 blastocysts via Micropipette Aspiration Assays. As expected, maternally aged blastocysts exhibited increased surface tension at the mural trophectoderm (Fig. 3c, ED. Fig. 3a, Supp. Movie 2). This increased surface tension indicates elevated mTE tissue tension, which could restrict tissue spreading during implantation.

In addition to elevated surface tension, an increase in cell contractility in embryos from aged females could also lead to stronger cell-substrate applied traction forces[41]. To measure cell-substrate forces during *in vitro* implantation[32], we embedded fluorescent beads in our synthetic substrate PAA gels (ED. Fig. 3b) and applied the biophysical technique of Traction Force Microscopy (TFM). Bead trajectories indicate the substrate deformation and can be used to calculate the applied traction stresses that result from cellular forces at cell-substrate adhesions[41,49,50]. TFM provides a powerful approach to determine the tissue's contractile state during implantation[32].

We observed a surprising age-related hyperactivation of contractility within the migrating trophectoderm front in aged embryos (Fig. 3d, Supp. Movie 3). Analysis of traction profiles across multiple samples revealed strong fluctuations in active traction forces. This observation was consistent with a recent study that reported intermittent tractions applied by mouse embryos on extracellular matrix[32]. For embryos of the same spread area, aged embryos showed an increase in total contractile work performed, consistent with hypercontractility in embryos of advanced maternal age (Fig. 3e). Maternally-aged embryos, in our *in vitro* implantation assay, exhibited a heightened contractile energy per unit spread area over 24 hours (Fig. 3f).

Our data indicate that the hypercontractility of embryos from aged females leads to an increase in both surface tension and cell-substrate tractions. To assess their impact on embryo spreading, we used our active wetting model (Fig. 3b), which is based on force balance, $\boldsymbol{\nabla}\cdot\boldsymbol{\sigma} + \boldsymbol{T}_{\mathrm{a}} = 0$, between cell-substrate active tractions $\boldsymbol{T}_{\mathrm{a}}$ and internal forces in the tissue, captured by its stress tensor $\boldsymbol{\sigma}$ (Supplementary Note 1). As in our measurements (Fig. 3d), our model assumes that tractions are maximal at the tissue leading edge and decay inwards with a decay length $L_{\mathrm{c}} \approx 15\ \mu\mathrm{m}$ (see Methods) (ED. Fig. 3c). Whereas similar traction patterns can emerge just from substrate adhesion in non-migrating contractile cell layers[51], our wetting model is consistent with both the traction pattern and the observed spreading. In the model, internal stresses are due to tissue flow $\boldsymbol{v}$ with viscosity $\eta : \sigma_{\alpha\beta} = \eta\left(\partial_\alpha v_\beta + \partial_\beta v_\alpha\right)$, where Greek indices denote spatial components. Moreover, following wetting theory, we account for the embryo's surface tension γ through a Young-Dupré condition at the tissue's leading edge: $\sigma_{rr}(R) = -\gamma\cos\theta$, where r denotes the radial component, R the spread radius, and θ the contact angle[48] (Fig. 3b, ED. Fig. 3d).

We then solved the model and fitted it to the area spreading dynamics of all embryos (Supplementary Note 1, ED. Fig. 3e, Supplementary Note 2). The results reveal that, in addition to higher surface tension (Fig. 3c) and higher tractions (Fig. 3g), aged embryos also exhibit a higher tissue viscosity (Fig. 3h), which contributes to slower spreading dynamics to hinder implantation. These analyses support the role of age-related alterations in tissue mechanics in driving defective embryo implantation.

To further validate our modeling results, we assessed the mechanical properties of the tissue using cell shape as a proxy for tissue viscosity[52]. Previous work established the dimensionless shape index q, defined as the ratio of the cell perimeter over the square root of its area, as an indicator of the mechanical state of a tissue[53,54] (Fig. 3i). For non-motile cells, values of q below the threshold $q_{\mathrm{c}} = 3.8$ indicate tissues that are behaving like a solid, with largely hexagonal cell shapes. Higher values of q indicate a fluid state of the tissue. Cells exhibiting higher shape indices exhibit more elongated and irregular shapes, which yields a lower tissue viscosity. To apply this approach, we analyzed cell shape indices of the mural Trophectoderm region in all embryonic conditions. In all cases, we found $q > 3.8$ (Fig. 3i), consistent with the tissue being fluid, as assumed in our model. However, in embryos from younger mothers, shape indices were on average higher, indicative of a lower viscosity that may facilitate spreading. In contrast, in aged embryos, shape indices were lower, suggesting a heightened tissue viscosity consistent with the fitted values from our wetting model. This

increase in tissue surface tension and viscosity appear to arise from hyperactivation of contractility, as CN03-treated young embryos phenocopied the aged condition (ED. Figs. 3f–g).

Together these data indicate that maternally aged embryos exhibited heightened actomyosin contractility that increases regional mTE surface tensions at the future implantation site. Higher cellular contractility leads to increases of mTE cell-medium surface tension (Fig. 3c), mTE cell-substrate tractions (Figs. 3d, 3g), and tissue viscosity (Fig. 3h–i). These data support an implantation defect arising from impaired blastocyst wetting, in which age-related changes in tissue mechanics hinder spreading.

Embryos from aged females exhibit stronger cell-substrate focal adhesions

During trophectoderm spreading, actomyosin generates contractile forces that are transmitted to other cells through E-cadherin–mediated cell–cell adhesions and to the substrate through integrin-based adhesions (Fig. 4a)[41,43,49–50]. Increased contractility enhances both traction generation and intercellular force transmission, as well as increasing tissue viscosity and ultimately modulating tissue spreading. To quantify how embryos from aged females differ in their ability to spread during implantation, we developed an approach to measure trophectoderm dynamics over time. Using time-lapse imaging, we extracted the contour of the spreading trophectoderm and computed local velocities along the embryo perimeter, enabling the generation of spatially-resolved velocity maps and kymographs (Fig. 4b).

Analysis of trophectoderm perimeter velocity revealed a significant reduction in spreading dynamics in embryos from aged females (Fig. 4c). Young embryos displayed efficient and coordinated wetting behavior, characterized by rapid outward expansion and sustained edge velocities. In contrast, aged embryos exhibited inefficient wetting, with reduced spreading area and diminished, spatially heterogeneous edge dynamics (Fig. 4d). These data suggest that increased force generation (Fig. 3d) does not necessarily translate into effective tissue spreading. These findings are consistent with a mechanical state of aged embryos in which increased contractility and adhesion enhance force transmission but limit tissue flow.

Contractile forces generated by actomyosin are transmitted across the tissue and couple to both cell–cell and cell–substrate adhesions[41,43,49–50]. As a result, traction stresses arise not only from forward protrusive migration but also from the maturation of integrin-mediated adhesions at the trophectoderm–substrate interface. Focal adhesions sense mechanical forces and, under increased tension, recruit proteins like Paxillin and grow in size[49–50]. Growth of focal adhesion complexes therefore demarcate sustained and increased pulling forces. Paxillin immunostaining in embryos from younger females revealed smaller, more nascent focal complexes indicative of adhesions under lower tension (Fig. 4f). In contrast, contractility was hyperactive in aged embryos, which exhibited longer and larger Paxillin-positive focal adhesions.

To gain insight into the mechanical basis of these spreading defects in embryos from aged females, we next examined the contributions of RhoA-mediated contractility to tissue behavior. We experimentally increased actomyosin contractility in Young embryos using

CN03 to elevate effective tissue viscosity and overall tissue mechanics (Fig. 4e). Young embryos treated with CN03 exhibited increased focal adhesion length at the trophectoderm–substrate interface, comparable to that observed in aged embryos (Fig. 4f).

To test whether altered tissue material properties are sufficient to impair implantation-associated spreading, we increased cell–cell adhesion by treating blastocysts with ResEcad, a cell-permeable compound that enhances E-cadherin protein expression in epithelial tissues (Fig. 4e)[43]. We used this compound to specifically vary tissue viscosity and thus tissue mechanics. Strikingly, embryos with elevated E-cadherin levels exhibited a significant reduction in spreading area, phenocopying the aged condition (ED. Fig. 4). In parallel, we observed an increase in focal adhesion length, consistent with enhanced force transmission at the substrate interface. This finding suggests that tissue viscosity and traction-generating adhesions are not independent control parameters but are mechanistically coupled in the early embryo.

Together, these results support a model in which increased contractility and strengthened cell–cell adhesion act in concert to elevate tissue surface tension, tractions, and viscosity, which act together to impair trophectoderm spreading and results in inefficient wetting during implantation.

Compaction metrics predict implantation potential in embryos from both young and aged females

Contractility acts as a key driver in multiple morphogenetic stages preceding implantation[8,27,28,55,56]. For example, at the 8-cell compaction stage, compaction proceeds as endogenous contractility flattens the embryo's outer surface[57]. Often considered the first major morphogenetic checkpoint in the embryo, the timing and extent of compaction is dependent on RhoA-mediated contractility, which is reflected in an embryo's morphology[30,57]. Embryonic compaction is critical for cells to integrate mechanical stimuli and initiate placental programming in the future trophectoderm lineage, which carries out implantation.[58–60] We sought to leverage morphogenesis as a metric to create a non-invasive classifier to capture an embryo's mechanical potential in implantation. The logic behind this experimental framework was: (1) mechanically competent embryos are more likely to accomplish full implantation, and (2) mechanical properties can be identified during Compaction at the 8-cell stage using non-invasive methods.

To perform morphokinetic analyses of preimplantation development, mouse embryos from young and aged females were cultured *ex utero* starting from the 2-cell stage onwards, similar to previous work[61]. We specifically examined developmental tempo, or the dwell time within each stage from the 4-cell, 8-cell, and to the 16- to 32-cell stage when the embryo cavitates for blastocyst formation (Fig. 5a, Supp. Movie 4). We define the initiation of each developmental stage as the resolution of cell division from the previous cell cycle, with the stage's resolution being the initiation of the next subsequent cell division. This approach enables us to assay the developmental timing of maternally aged embryos and document alterations in morphogenesis that may underlie age-associated infertility.

Time-lapse imaging revealed a significant abbreviation of the 8-cell stage in embryos from aged females. In embryos from younger females, the dwell time during compaction stages was 9.5 hours on average, consistent with previous work assessing developmental tempo during the 8-cell stage[57]. In contrast, maternally aged embryos accelerated through the 8-cell stage an average of two hours faster than younger control embryos (Fig. 5a, ED. Fig. 5a). While we also find an age-dependent lengthening of the period to cavitation, we find no significant differences in total developmental timing between young and aged maternal conditions (ED. Fig. 5a).

We confirmed contractility at the 8-cell stage using the direct mechanical measurement of cortical tension via micropipette aspiration (Fig. 5b, Supp. Movie 5)[57,62]. As predicted by their accelerated progression through the 8-cell stage, maternally aged embryos showed significantly increased cortical tensions compared to young control embryos post-compaction (Fig. 5b). These data reveal an accelerated developmental tempo in embryos from advanced maternal age, leading to precocious compaction driven by aberrant cytoskeletal dynamics and heightened cortical tension in 8-cell stage embryos.

We hypothesized that this mechanical signature at compaction stages would be indicative of later trophectoderm function and outcomes during implantation. In this experimental scheme, we first harness the natural heterogeneity within embryos' compaction timing to generate a classifier that is predictive of implantation outcomes *in vitro* (Fig. 5c). To link compaction metrics of each embryo to its implantation outcome, we modified our *in vitro* implantation assay by culturing embryos on silicone grids so that each embryo could be indexed (Fig. 5d). Cultured embryos were imaged at 5-minute intervals from the 4- to the 16-cell stage, after which we calculated compaction metrics before processing indexed embryos for downstream *in vitro* implantation assays. We segregated embryos for implantation assays by two temporal conditions: 1) compaction timing >9 hours, similar to the younger control embryos, and 2) compaction timing <7.5 hours, similar to the maternally aged condition (Fig. 5e, Supp. Movie 6). Within these two binned conditions, we also measured the blastomere contact angles as a metric for each embryo's contractile state and endogenous cellular force balance (ED. Fig. 5b).

Two interconnected mechanical parameters at the 8-cell stage were predictive of implantation potential in our extended pre- and peri-implantation culture. We observed that the trophectoderm outgrowth spread area at late blastocyst stage correlated with the earlier developmental tempo over the period of compaction (Fig. 5f) as well as with the average inter blastomere contact angles just before cell division into the 16-cell stage (ED. Fig. 5c). Embryos that exhibited accelerated compaction and more acute cell-cell contact angles were statistically more likely to restrict spreading of their trophectoderm, resulting in reduced implantation potential *in vitro*. These correlations held for embryos from both young and aged mothers, enabling us to harness natural compaction heterogeneity to generate a classifier that is predictive of outcomes during *in vitro* implantation (Figs. 5g–h, ED. Fig. 5d). While earlier mechanical differences linked to implantation defects become more common at advanced maternal age, our results highlight the value of leveraging developmental tempo to identify implantation-competent embryos.

Embryos from aged females exhibit trophectoderm-specific cell fate defects

Previous studies have shown that lineage specification in the preimplantation embryo is tightly coupled to actomyosin contractility, polarity establishment, and Hippo/YAP signaling at compaction stages, where they regulate expression of key downstream transcriptional regulators of trophectoderm fate such as Cdx2[25,26,29–31,57–60,62]. Given the established role of mechanosensitive YAP signaling in lineage specification, we next examined whether heightened contractility is associated with alterations in YAP activity.

Consistent with reduced trophectoderm competence, compaction-stage aged embryos exhibited significantly decreased nuclear YAP localization compared to young controls (Fig. 6a). This reduction in YAP activity was accompanied by a corresponding decrease in Cdx2 expression at the blastocyst stage (Fig. 6b–d). Together, these results suggest that early mechanical alterations are associated with impaired activation of YAP-dependent transcriptional programs, leading to reduced trophectoderm differentiation potential.

Cell position (outer versus inner cells) is a strong determinant of trophectoderm versus inner cell mass fate in the early embryo. We asked whether the mechanical alterations in embryos from older females biased their position in the embryo. To highlight age-related positional biases, we performed a competition between young and aged embryos by generating heterochronic chimeras in which we aggregated membrane-GFP and H2B-Halo labeled, injected blastomeres from young embryos with unlabeled host embryos at the 8-cell stage and assessed their contribution to inner cell mass (ICM) and trophectoderm (TE) lineages at the blastocyst stage (Fig. 6e, Supp. Movie 7).

Heterochronic chimeras provide reveal intrinsic differences in lineage competence that can be more subtle in whole-embryo analyses. By forcing cells to compete, this approach amplifies subtle asymmetries and allows both cell-autonomous and collective effects to emerge. While mechanotransduction pathways such as YAP signaling bias fate decisions within individual cells, differences in mechanical properties can also drive sorting between neighboring cells. Thus, chimeras link early mechanical differences to both lineage specification and spatial organization, providing a functional readout of how mechanics shapes developmental outcomes.

In control chimeras composed of age-matched young embryos, labeled cells contributed comparably to both ICM and TE compartments. In contrast, when cells derived from aged embryos were introduced into a young host environment, they exhibited a marked bias away from the TE lineage and were preferentially localized to the ICM (Fig. 6f–g). These findings indicate that cells from aged embryos are impaired in their ability to adopt or maintain trophectoderm identity, even in a permissive environment. Importantly, because chimeras are generated at the 8-cell stage (prior to overt lineage segregation), these results indicate that the bias in lineage allocation originates at or before compaction. Thus, these data provide functional evidence linking early differences in cell state to downstream fate decisions. Furthermore, this approach allows us to capture not only cell-autonomous effects, such as altered mechanotransduction (e.g., YAP signaling), but also emergent behaviors arising from interactions between cells. In particular, the preferential localization of aged cells reflects both reduced trophectoderm competence and a mechanically driven sorting process (which

itself could alter cell fate determination), highlighting how differences in cellular mechanical properties can influence both fate and spatial organization. While we cannot fully separate fate-driven positioning from mechanically driven sorting, chimeras demonstrate that both processes originate from intrinsic differences established as early as the 8-cell stage.

Notably, these fate defects emerge downstream of the compaction stage, a developmental window in which we observe pronounced changes in tissue mechanics. Although compaction precedes overt spatial segregation of TE and ICM lineages, it represents a critical period during which mechanical cues can influence subsequent cell fate decisions. Our findings support a model in which altered mechanical properties at the 8-cell stage bias cell position, impairing lineage allocation through mechanosensitive pathways and resulting in reduced trophectoderm specification.

Human embryos display age-associated mechanical signatures

To test whether the mechanical defects identified in mouse embryos were conserved in humans, we analyzed donated human blastocysts generated through standard IVF procedures and binned them by maternal age. Human embryos undergo implantation through similar yet distinct mechanisms to mouse embryos, with human embryo implantation occurring at the polar trophectoderm (pTE) region proximal to the ICM (Fig. 1a)[32]. Immunostaining for phosphorylated Myosin Light Chain (pMLC), the canonical marker of actomyosin contractility, reveals a significant age-associated increase in junctional pMLC intensity within the polar trophectoderm region (Figs. 7a–b). Elevated pMLC at the polar trophectoderm region parallels the hypercontractility observed in the implantation site (mural trophectoderm) in aged mouse embryos (Fig. 3c). These data suggest that advanced maternal age enhances actomyosin activity in the trophectoderm lineage, increasing tissue tension at the future implantation interface for both humans (pTE) and mice (mTE).

We then assessed whether changes in cytoskeletal contractility translate into altered cell and tissue viscosity of the polar trophectoderm region, using the dimensionless shape parameter q as a proxy. Using the immunostaining of fixed embryos for trophectoderm junctions labeled for ZO-1, we segmented individual cell outlines and quantified the dimensionless shape index (Figs. 7c–d). As in mouse blastocysts (Fig. 3i), human embryos from younger mothers display higher average q values, indicative of a more fluid-like, deformable tissue state. Embryos from older mothers show lower q values, consistent with increased viscosity and reduced epithelial fluidity. Notably, elevated pMLC intensity is highly consistent with the low shape index values at the polar trophectoderm region, linking biochemical markers of contractility to emergent geometric signatures of tissue mechanics.

We next asked whether this heightened contractility in human embryos is accompanied by altered morphokinetics that can be assayed through non-invasive live imaging, similar to our timelapse data on mouse embryo compaction (Fig. 5). We analyzed de-identified timelapse imaging data of preimplantation embryo development from individuals undergoing Assisted Reproductive Technologies using the Embryoscope. The Embryoscope is an FDA-approved microscope and incubator system that enables acquisition of brightfield z-stack timelapses spanning from the 2-cell to the blastocyst stage, after which embryos are individually selected for uterine transfer and recorded for their pregnancy outcomes.

Embryos were divided into two groups: (1) *Young embryos*, derived from oocytes of women under 28 years of age and transferred to older surrogate recipients (>40 years), and (2) *Aged euploid embryos*, derived from oocytes of women over 40 years of age and transferred to similarly older female recipients (Fig 7e). The rationale behind these two groups was to compare embryo morphokinetics between Young and Aged embryos with known implantation outcomes. Importantly, we identified Aged euploid embryos to remove confounding factors of potential genetic aneuploidies in resulting implantation outcomes. To assess whether these morphokinetic signatures correlate with implantation competence, we linked compaction timing to known clinical outcomes following embryo transfer: Group 1 Young embryos, upon uterine transfer, yielded full pregnancy and successful live births, while Group 2 Aged embryos displayed a failure in implantation with no live birth.

Quantitative analysis of developmental tempo revealed that embryos from women >40 years old exhibit accelerated time from the start of the 8-cell stage to initial compaction compared to embryos from younger patients (Figs. 7f–g, Supp. Movie 8). Here, initial compaction was demarcated by the disappearance of the optical contrast of cell-cell boundaries, indicative of increased actomyosin contractility and adhesive engagement. This relation persists even after controlling for blastocyst euploidy status, underscoring that mechanical tempo is a possible independent predictor of implantation potential. Similar to the murine classifier (Fig. 5), compaction timing is predictive of implantation competence in human embryos, suggesting that the age-associated mechanical state of the embryo can be inferred from morphokinetic features.

Discussion

In this study, we uncover a core mechanical defect in embryos from aged females that underlies their impaired implantation competence. We leverage this knowledge to identify the small subset of embryos from older mothers that are competent for implantation. Using mouse models, we find that maternal reproductive aging triggers an increase in contractility in the extra-embryonic trophectoderm, decreasing the ability of these embryos to implant both *in vivo* and *in vitro* (Figs. 1, 3, 4). Enhanced contractility is both necessary and sufficient to drive the age-related defects of implantation failure (Fig. 2). Contractility acts to increase effective tissue viscosity, impairing implantation of embryos from older females through enhanced force transmission at adhesions (Fig. 3, 4). Furthermore, non-invasive assays for altered mechanics (timing of embryo compaction, blastomere contact angles, direct physical measurements) can predict the embryos that are most likely to lead to successful implantation in both young and older mothers (Fig. 5). Early hypercontractility at compaction induces a dampening of trophectoderm specification (Fig. 6). The maternal age-related increase in mouse embryo contractility is also observed in human embryos (Fig. 7). This work implicates embryo mechanics as a key regulator of female reproductive longevity. (Fig. 8).

We observe heightened mechanics in embryos of both aged humans and mice. Maternal age was associated with a marked elevation in junctional phosphorylated myosin within the polar trophectoderm, the lineage that interacts with the human maternal endometrium. This age-associated hypercontractility mirrors the mural trophectoderm phenotype observed in

aged mouse blastocysts, indicating that heightened contractile tissue tension is a hallmark of reproductive aging across mammalian species. We also leverage continuous time-lapse imaging in the Embryoscope. Here, the earliest stages of human embryogenesis similarly harbors alterations in contractility that mirrored those seen in mice. This shift in mechanical tempo, or the rate at which cells flatten and establish cohesive epithelial architecture, is strongly associated with diminished implantation competence, even after controlling for ploidy.

Compaction morphokinetics are not simply a measure of developmental tempo but rather serve as a proxy for the tensional landscape of the embryo[57]. Compaction is the first mechanical transition in preimplantation development. During compaction, actomyosin contractility increases, cell-cell adhesion strengthens, and polarity is established in a coordinated manner[25,26,29–31,57–60,62]. Our findings suggest that age-associated hypercontractility at this stage may preconfigure the mechanical state of the trophectoderm lineage. We note that the altered lineage contribution observed in heterochronic chimeras could arise through multiple, non-mutually exclusive mechanisms. Differences in mechanical properties may drive physical sorting of cells within the embryo, thereby influencing their final position and subsequent fate. Alternatively, early changes in mechanotransduction could bias lineage specification in a cell-autonomous manner, with positioning emerging as a consequence of fate. Because chimeras are generated at the 8-cell stage, prior to overt lineage segregation, the observed bias must originate from intrinsic differences established at or before compaction. Furthermore, the reduction in nuclear YAP-associated gene expression in aged embryos supports a model in which mechanosensitive signaling pathways are altered early, biasing lineage competence. Together, these findings suggest that early mechanical differences act both to bias cell fate and to promote mechanically driven sorting, coupling lineage specification and spatial organization during development. These results establish a developmental link between early mechanical dysregulation at compaction, altered cell fate decisions, and the functional deficits observed at the time of implantation.

Understanding the cell biological origins of age-associated infertility is critical for improving embryo selection of the small pool of maternally aged embryos that are capable of uterine integration. Current embryo screening methods in IVF remain limited: morphological grading is subjective and often inconsistent between clinics, while preimplantation genetic testing for aneuploidy (PGT-A) does not provide a definitive diagnosis of the genetic status of the fetus proper[7,14,15,20,22,23,63]. Although chromosomal abnormalities are common with maternal age, even euploid embryos still frequently fail to implant, indicating that genetics alone cannot fully capture embryonic competence[7]. Mechanics may provide this missing dimension; cytoskeletal organization and tissue-level force balance not only regulate morphogenetic behaviors essential for implantation but are also increasingly recognized as upstream modulators of ploidy stability via cytoskeletal pathways[27,64]. Evidence from oocyte biology suggests that maternal age compromises cytoskeletal integrity, initial spindle positioning, and microtubule stability, potentially contributing to errors in chromosome segregation[8,9]. Thus, non-invasive mechanical screening of embryos could complement current morphology- and genetics-based assessments by capturing functional viability at the level of tissue dynamics.

Our findings extend prior studies of mechanics-based morphogenesis defects for pre-implantation mouse and human embryos[62]. This previous work demonstrated that the 8-cell compaction stage represents a mechanical checkpoint where cortical tension and adhesion are integrated to establish blastomere flattening and robust blastocyst morphogenesis[57]. However, these obvious compaction defects are captured in existing embryo grading schemes[2]. Our work focuses on the critical process of implantation, for which there were no strong predictive metrics in the IVF field. The abbreviated compaction we observe in mouse embryos from aged females defines a distinctive mechanical signature that predicts implantation competence, forming the foundation for objective screening tools that may improve IVF outcomes for patients of all ages, especially given that these age-associated defects are also observed in human embryos.

We identify hypercontractility as a core embryonic defect underlying age-related implantation failure, but the molecular basis of this mechanical abnormality is not known. The origins of this hypercontractility are likely multifactorial and may begin well before fertilization. While the aged uterus may be competent for embryo implantation, this does not rule out a maternal source of age-related alterations in egg quality. Importantly, the ovarian environment undergoes profound age-related remodeling[65,66]. The aging ovarian microenvironment is characterized by increased fibrosis, stromal rigidity, and altered extracellular matrix organization—changes that impair follicle development and oocyte quality[5]. Indeed, ovarian stiffness increases with age and directly influences follicle mechanics and oocyte maturation. These findings suggest that embryos from older females may inherit latent biomechanical liabilities established during oogenesis in a stiffened ovarian niche that could persist through cleavage divisions to compromise implantation. Alternatively, age-related changes in contractility may be a genetic hallmark of aging, as seen in other contexts such as stem cell niches[67].

These data presented here carry several translational implications. First, they suggest that embryos selected solely on genetic normalcy may still harbor latent mechanical defects that compromise implantation, offering a potential explanation for the frequent discordance between euploidy and clinical success. Second, they highlight compaction timing as a practical biomarker that can be extracted from existing Embryoscope datasets, enabling retrospective validation and prospective implementation without altering clinical workflow. Finally, they point toward the possibility that restoring proper mechanics (i.e. culture optimization, modulation of cytoskeletal behavior, or new mechanical-screening technologies) could improve outcomes for patients of advanced maternal age. Indeed, previous work showed that aged mouse oocytes, when transplanted to ovarian follicles from younger female mice, show markedly improved pregnancy success[68]. Additionally, reducing ovarian microenvironment stiffness via antifibrotic drugs is also associated with improved developmental outcomes[69]. Together, these data highlight the potential for rejuvenation in reproductive aging, offering renewed hope for rescuing developmental potential in embryos of older women. Our work potentiates similar translational tools that not only identify implantation-competent embryos but also build platforms for rescuing embryonic implantation.

Materials and Methods

Ethics statement

All research was conducted in accordance with relevant institutional, national, and international regulations and guidelines. Animal experiments were performed at the University of California, San Francisco (UCSF) and approved by the UCSF Institutional Animal Care and Use Committee (IACUC; Protocol AN197455). Human embryo studies were conducted at Stanford University using supernumerary embryos donated for research through the Stanford RENEW Biobank (IRB 10466) and were approved by the Stanford Human Subjects Research Compliance Office under protocols SCRO 929 and IRB 72398. All human embryo research was performed in accordance with California Department of Public Health guidelines, CIRM regulations, and the ISSCR Guidelines for Stem Cell Research and Clinical Translation (2021). De-identified human Embryoscope datasets were obtained and analyzed under protocols approved by the Northwestern University Institutional Review Board.

Ethics Statement - Human Embryos

In this research study, we used a total of 4 human embryos at blastocyst stage (5 d.p.f.), and one aged embryo was discarded from analyses because it was unintentionally destroyed in the staining process. Aged embryos were both female from the same patient of age 43. Young embryos contained one male and one female from a patient who was 30 years old. All embryos were euploid. This was the minimum number of embryos required to collect the molecular and cellular data presented in this article. Samples were stored in 4C in PBS and saved for future analyses. Human embryo material is subject to donor consent and institutional restrictions and cannot be transferred to other investigators. Experiments conducted at Stanford were performed in accordance with California Department of Public Health (Guidelines for Human Stem Cell Research Pursuant to Health and Safety Code 125118, updated April 2018) and CIRM Regulations (Chapter 2. Scientific and Medical Accountability Standards, § 100030, Activities Not Eligible for CIRM Funding, updated 08/21/17)). Only supernumerary embryos have been used, recruited by the Stanford RENEW Biobank (IRB 10466). Experiments were performed under protocols SCRO 929 and IRB 72398 approved by the Stanford Human Subjects Research Compliance Office. All embryo cultures at Stanford were stopped by 12 days or before the appearance of the primitive streak (whichever is earlier). All experiments were conducted in a research building independently funded by the California Institute for Regenerative Medicine, and no federal funding was used for these experiments. The evaluation and approval of this research through a specialized scientific and ethics review process complies with the International Society for Stem Cell Research (ISSCR) Guidelines for Stem Cell Research and Clinical translation (2021). Specifically, that the research has a compelling scientific rationale that necessitates the use of embryos and that the minimum number of embryos to achieve the scientific objectives were used. All material was donated and participants did not receive compensation. Informed consent was obtained from all couples who donated their supernumerary embryos following IVF treatment. Before giving consent, donors were provided with full information about the research project and objectives, potential risks and benefits, that participation to donate their embryos is voluntary and they can

withdraw from the study at any time, how their information will be used, and they had the opportunity to receive counseling before agreeing donation. Donors were fully informed that embryo cultures would be stopped by 12 days post-fertilization in the US, that subsequent biochemical and genetic studies would be performed on the samples, and that the results of these will be published in scientific journals. No financial inducements were offered for donation. Before the start of each experiment and thawing of an embryo, we verify that patients' consents continue to be valid and that consent has not been withdrawn. Embryoscope time-lapse data were de-identified and exported from the Fertility Clinic at Northwestern University's Center for Reproductive Science under a protocol approved by the institutional review board. All exports were performed by clinical staff not involved in downstream analysis. De-identified datasets were stored on encrypted institutional servers and accessed only by authorized research staff under IRB oversight. Data was retrospective so no ethics oversight is needed.

Public Data on IVF Uterine Transfers

Surrogacy data was collated from the Human Fertilisation and Embryology Authority (HFEA)[24]. HFEA data was chosen for it being the most complete IVF dataset that included uterine transfers with aged female surrogates from aged female egg donors. Uterine transfers were selected and binned based on the age of the surrogate female and the age of the embryo donor. Young women were considered less than 35 years of age and aged women were considered over 35 years of age. Only eggs that were donated within specific binned maternal age categories were considered for downstream analyses. In this way, we excluded patient's own eggs. Live birth rates from years 2012 to 2022 were then calculated as the birth rate per number of embryos transferred. Live birth rates were then averaged over the decade to give an averaged live birth rate for each transfer condition.

Animal husbandry and Mouse lines

B6C3F1/J males were acquired from The Jackson Laboratory (Cat#100010) at 6 weeks of aged and utilized as male studs for breeding until 35 weeks of age. Vasectomized CD1 males were acquired from Charles River (Cat#022) at 6 weeks of age and 7-days post operation with sutures removed. CB6F1 females were used for breeding in two aged conditions: 6-9 weeks of age and 40 weeks of age. Young control CB6F1 females were acquired from The Jackson Laboratory (Cat#100009) and aged CB6F1 female mice were acquired through the National Institutes of Aging or acquired from the Jackson Laboratory (Cat#100009) and aged in house. Mice were housed on a 12 hour light:dark cycle and animal facilities were maintained at 21C. All animal work was carried out at the University of California, San Francisco (UCSF). Animal husbandry was performed in accordance with the UCSF Laboratory Animal Resource Center (LARC) guidelines. All experimental procedures were approved by the UCSF Institutional Animal Use and Care Committee (IACUC Protocol AN197455). Mice were housed in a specific pathogen-free facility on a 12 h light:12 h dark cycle at an ambient temperature of 21 °C and a relative humidity of 30–70%, with food and water provided ad libitum.

Human Embryo Thawing and Culture

Supernumerary human blastocysts cryopreserved at 5 d.p.f. were thawed using Vit Kit-Thaw by Irvine Scientific (Fujifilm, Cat#90137-SO). Open-pulled straws containing vitrified blastocysts were transferred directly from liquid nitrogen into 1 mL pre-warmed thawing solution (TS). After 1 minute immersed in TS, blastocysts were transferred at room temperature consecutively into 60uL drops of the following solutions Dilution Solution (DS, 3 minutes), Washing Step 1 Solution (WS1, 4 minutes), Washing Step 2 Solution (WS2, 4 minutes). After these steps, each blastocyst was then transferred to one well of a 96well plate containing 100uL of Embryo Culture Medium SAGE 1 (Origio, Cat#67010060A) supplemented with 5% Human Serum Albumin (Vitrolife, Cat#10064) and incubated for $\tilde{2}$ hours at 37°C, 20% O2 and 5% CO2 to allow time for recovery after thawing. After recovery from thawing, each blastocyst was then transferred to one well of a 96well plate containing 200uL of Human Embryo Medium. The composition of HEM1 containing the following: Advanced DMEM/F12 (Gibco, Cat#12634-010) supplemented with 1 x B27 (Gibco, Cat#12587-010), 1 x N2 supplement (Gibco, Cat#17502-048), 2 mM L-glutamine, 0.2 % Penicillin-Streptomycin (10000 U/mL, Gibco, Cat#15140122), 1.25 mM N-Acetyl-L-cysteine (NAC, Sigma, Cat#A9165), 10 mM46 Nicotinamide (Sigma, Cat#N0636), 2% charcoal stripped FBS (Sigma Aldrich, Cat#F6765), 5% Human Serum Albumin (Vitrolife, Cat#10064), 0.5 mg/mL hyaluronan (Abcam, Cat#Ab143634), 10 nM β-oestradiol (E2), 1 μM progesterone (P4), 20 ng/mL Prolactin (Peprotech Cat#100-07), 1 μg/mL human Chorionic Gonadotropin (hCG, RP-1484, Alpha Diagnostic Intl) and 20 ng/mL human Placental Lactogen (hPL, R&D Cat#5757-PL/CF), 50 ng/mL 1 IGF-1 (Cell Guidance Systems Cat#GFH34AF) and 50 ng/mL epidermal growth factor (EGF, Peprotech, Cat#AF-100-15). Blastocysts were cultured at 37°C, 20% O2 and 5% CO2. until fully expanded (6-7d.p.f.) and then fixed in 4% PFA for 15 minutes on ice. After fixation blastocysts were transferred to PBS and kept until immunofluorescence was performed

Mouse Embryo Collections

Females were superovulated with 5IU PMS-G (Ilex A22721) at Day 1 and 5IU hCG (Ilex A225005) on Day 3, upon which they were placed with male studs for breeding. Copulation plugs were assessed on Day 4, and oviducts were surgically removed on Day 5 to collect embryos at E1.5 (2-cell stage). Oviducts were manually flushed using a blunt needle with EmbryoMax KSOM-AA Medium (EMD Millipore Cat#MR-101-D) to isolate embryos. Only phenotypically healthy 2-cell staged embryos were used for downstream assays; embryos were discarded if they showed severe fragmentation or malformation. Embryos were then washed in consecutive drops of KSOM-AA covered in Fijifilm light mineral oil (Fujifilm Cat#9305) before moving them to precalibrated drops of KSOM-AA under mineral oil. Embryos were incubated for culture in 37C, 5% CO_2 conditions.

NSET Procedures

Female surrogate mice of specified ages were superovulated as stated above. Embryos were collected at E1.5 and cultured until E3.5 Blastocyst stages. Recipient females were mated in parallel with vasectomized males and checked the next day for copulation plugs to confirm mating. Pseudopregnant females were timed for downstream use for NSET for

2.5 days post-coitum. E3.5 blastocysts were pooled and transferred using mNSET Devices for Mice (ParaTechs Corporation Cat#60010). Blastocysts were transferred in groups of 7-12 embryos to each recipient female to not overload each uterine horn. Surrogate females were monitored for distress for 3 days and again assessed for litter births 21 days post NSET procedure. NSET success was assessed as number of pups born divided by transferred blastocysts to calculate percentage of live births.

In vitro Implantation Assays

In vitro implantation assays used were optimized from previously published reports[40]. In brief, embryos were collected at E1.5 and cultured until E3.5 blastocysts. Blastocysts were denuded using Acidic Tyrode's solution (Sigma-Aldrich Cat# MR-004-D) until the zona pellucida was dissolved. Embryos were then transferred to KSOM-AA to deactivate any leftover Tyrode's solution. In the event the zona pellucida was not fully removed, it was mechanically removed using a blunt glass pipette and manual pipetting. Blastocysts were then transferred to a 24-well plate (Corning, Cat#3526) with IVC media with 1:2000 dilution of SPY650-FastAct (Cytoskeleton Cat#CY-SC505) to begin incubation at D0. IVC media contained 1mg/mL Progesterone (Sigma-Aldrich Cat#P0130), 10μm Beta-estradiol (Sigma-Aldrich Cat#E2758-250MG), and 50mM N-Acetyl-L-cysteine (Sigma-Aldrich Cat#A7250) in advanced DMEM/F-12 (Life Technologies Cat#12634-010) supplemented with 25% ESC-grade Fetal Calf Serum (Life Technologies Cat#10439001), 1% ITS-X (Life Technologies Cat#51500-056), 1% Glutamax (Life Technologies Cat#35050-061), and 0.25% Pen/Strep (Gibco Cat#15140122). On Day 1, blastocysts were subsequently transferred to 6-well plates or Chamlide Chambers (Live Cell Instruments Cat#CM-M25-4) containing collagen-coated Polyacrylamide gels with fresh IVC media and SPY650-FastAct to enable live imaging of embryo implantation and/or Traction Force Microscopy. For immunostaining to analyze trophectoderm outgrowth, embryos were fixed as described in specific experimental workflows.

Drug treatments

Embryos were treated with the cell-permeable drugs listed below starting at the late 2- to 4-cell stage before downstream applications. Control and drug-treated embryos were cultured each in a well from a 24-well plate (Corning, Cat#3526) in the absence of light mineral oil. Embryos were treated with equilibrated KSOM-AA and/or IVC media containing 1μg/mL RhoA Activator II (Cytoskeleton Cat #CN03) or 10μM Ripasudil (Selleck Chemical Cat#50-136-6407) or 10 uM ResEcad (Sigma-Aldrich Cat#205615). Control embryos were treated with the same amount of vehicle (DMSO or water). Drugs were reconstituted according to manufacturer's instructions before dilution to working conditions in KSOM-AA.

Immunofluorescence

For blastocysts, embryos were placed in microbubbles with stated reagents on Greiner Bio-One Terasaki Plates (Cat#07-000-658) for all staining protocols. Gel-implanted embryos on glass coverslips were stained in 6-well dishes for all staining protocols. Embryos and coverslips were fixed in 4% PFA (Electron Microscopy Sciences Cat#15700) in PBS solution (Corning) at Room Temperature. Embryos were removed from PFA and then

washed 3 times for 5 minutes each in PBS with 0.05% Tween-20 (PBST). Permeabilization was achieved through 0.3% Triton X-100 in PBS solution for 20 minutes and subsequently washed four times, 5-10 minutes each in PBST. Embryos were then blocked in blocking solution of 10% FBS diluted in PBST for 4 hours at room temperature. Antibodies were diluted in blocking solution and incubated overnight at 4C. Embryos were washed again three times for 10 minutes in PBST before being placed in secondary antibody solution with antibodies and DAPI diluted in blocking buffer. Embryos were incubated for 2 hours in secondary antibodies, washed four times in 10-minute PBST washes. Blastocysts were then transferred to a microbubble of PBS on a glass-bottomed MatTek dish (MatTek Corporation, P35G-1.5-20C) for downstream imaging. For gel-implanted embryos, glass coverslips were mounted with 10uL ProLong Gold (Invitrogen Cat# P36930) before being cured and sealed with nail polish. Immunostained blastocysts and coverslips were then stored at 4C before imaging. Human blastocysts were permeabilized in PBS containing 0.3% Triton X-100 and 0.1 M glycine for 15 minutes at room temperature. Samples were then blocked in blocking solution: PBS containing 10% FBS, 2% bovine serum albumin (BSA), and 0.1% Tween-20 for 1 hour at room temperature. Samples were then incubated overnight at 4°C in primary antibodies diluted in the above blocking solution (details below). The following day, samples were washed in PBS with 0.1% Tween-20 and incubated for 2 hours at room temperature protected from light with fluorescently conjugated secondary antibodies and DAPI diluted in blocking solution. Samples were stored at 4°C in PBS.

Antibodies

Primary antibodies used were: Rabbit pMLC (1:200; Cell Signaling Cat#3671S), Mouse ZO-1 clone 1A12 (1:200; Invitrogen Cat#33-9100), Goat ZO-1 (1:200; Invitrogen Cat#PA5-19090), Rabbit VD7 (2mg/ml, a kind gift from Dietmar Vestweber lab), Rabbit ppMLC (1:200; Cell Signaling Cat#3674T), Mouse Alpha-catenin clone 7A4 (1:500; Thermo Fisher Cat#13-9700), Rabbit NMIIA (1:200, BioLegend Cat#909802) Rat NMIIB (Abcam Cat# (EPR22564-23), Rabbit NMIIB (BioLegend Cat#909902), Mouse Paxillin (1:200; BD Biosciences Cat#610051), Rabbit pMLC (1:200; Cell Signaling Cat#3671S), Rabbit YAP (1:100; Cell Signaling Cat#14074), Mouse Cdx2 (1:200; Biogenex Cat#MU392A-5UC); Rabbit Sox2 (1:200; Millipore Signa Cat#AB5603), Goat Sox2 (1:100; R&D Systems Cat#AF2018). Secondary antibodies used were Alexa Fluor Goat anti-Mouse 647 (1:300, Invitrogen Cat#A21235), Alexa Fluor Goat anti-Mouse 568 (1:300, Invitrogen Cat#A11031), Alexa Fluor Goat anti-Rabbit 568 (1:300, Invitrogen Cat#A11055), Alexa Fluor Donkey anti-Rabbit 647 (1:300, Invitrogen Cat#A31573), Alexa Fluor Phalloidin 488 (1:100; ThermoFisher Cat#A12379), and DAPI (1:100, Sigma-Aldrich Cat#MBD0015).

Calculating Junctional Intensity Levels of Tension-associated proteins

Junctional intensities of NMIIA, NMIIB, pMLC, alpha-catenin, and VD7 were calculated in Imaris and Excel. Surface renderings were performed using machine learning segmentation in the ZO-1 channel as a reference to isolate total junctions of the blastocyst. Junctions were virtually cut at cellular vertices to further isolate single cell-cell junctions along their length. Blastocysts' junctions were then binned based on their presence at either polar or mural trophectoderm regions using the classification tool. Mean intensities of constituent

channels were extracted using Imaris Statistics. Ratiometric values was then calculated for each junction using excel. For myosin levels, all channels were normalized to ZO-1 intensity levels. VD7 intensities were normalized to total alpha-catenin levels.

Fluorescence intensities of nuclear markers

Nuclear protein intensities were quantified using FIJI (ImageJ, NIH). Confocal z-stacks were first converted into sum intensity projections using the *Z Project* function (Sum Slices) to preserve total signal across the nucleus. All images within an experiment were processed using identical projection parameters. Nuclei were identified based on DAPI signal, and regions of interest (ROIs) corresponding to individual nuclei were generated using automated thresholding followed by watershed segmentation to separate closely apposed nuclei. ROIs were manually curated to ensure accurate nuclear boundaries and exclude debris or improperly segmented regions. For each ROI, integrated intensity and area were measured from the corresponding protein channel. Nuclear intensity was calculated as mean intensity (integrated intensity divided by ROI area) to account for differences in nuclear size. Background signal was measured from cell-free regions within each image and subtracted from all nuclear measurements.

Cell shape analysis

Mural Trophectoderm cell shapes were taken from fixed samples using the ZO-1 imaging channel. Imaging stacks were resliced using FIJI's reslice tool to orient the bottom 1/3rd region of the mTE and projected into a single en face plane. Image analysis to isolate cell shapes was performed in Python to extract cell perimeters and area only in the middle region of the 3D projection so as to not include any potentially stretched cells at the periphery.

Average focal adhesion length measurements

Focal adhesions were quantified from paxillin immunofluorescence images using Imaris (Bitplane, Oxford Instruments). Image stacks were imported into Imaris and preprocessed using background subtraction and Gaussian smoothing to reduce noise while preserving adhesion structures. Paxillin-positive adhesions were segmented using the *Surfaces* module. Thresholding parameters were set based on intensity to identify discrete paxillin-enriched regions corresponding to focal adhesions. A minimum size filter was applied to exclude small, non-specific puncta. Segmentation parameters were kept consistent across all conditions within each experiment. Identical segmentation thresholds and filtering parameters were applied across all samples within each experiment. For each detected adhesion, geometric features including length were extracted using the Imaris measurement tools. Adhesion length was defined as the longest axis of the segmented object. Measurements from all adhesions within a given embryo were pooled to calculate the average focal adhesion length per embryo. These values were then used for downstream statistical analysis. All segmentation and quantification were performed blinded to experimental condition.

Calculating trophectoderm spreading and velocity

To analyze trophectoderm spreading, the 650-FastAct channel was used. Only the plane of tissue-substrate adhesion was used to calculate spread area. 650-FastAct was then thresholded in ImageJ to generate an actin mask and then particle analyzed to generate distinct Regions of Interest for each timepoint. ROIs were then measured in ImageJ and values were exported to Excel. The start of implantation was marked as T0 with the appearance of protrusive cells that made a stable blastocyst-substrate attachment that then expanded into an outgrowth. We then computationally isolated the perimeter edge and assigned each coordinate point a corresponding calculation of its velocity. Each point along the migrating front's perimeter was then color coded corresponding to its velocity measurement. Upon normalizing the length of each embryo's spreading trophectoderm perimeter to 1, we create kymographs of the trophectoderm's contour mapping average velocity over the 24 hour implantation period. Kymographs of trophectoderm outgrowth velocities were then calculated using ADAPT ImageJ plugin. Masks of trophectoderm outgrowths were used as inputs for the ADAPT plugin to generate individual kymographs of each implanting blastocyst. Each kymograph was then calculated for average fluorescence to calculate average velocity of the outgrowth.

Chimera generation and quantification

Embryos were collected at the 2-cell stage and maintained in KSOM culture medium under mineral oil under standard culture conditions. Microinjections were performed using a micromanipulation system equipped with a FemtoJet microinjector (Eppendorf) and micromanipulators mounted on a Leica DMi8 manual microscope with Integrated Modulation Contrast and Phase Contrast with Eppendorf Micromanipulators and Femtojet 4i. Embryos were microinjected using an Eppendorf FemtoJet system. Capped mRNA encoding membrane-GFP (100ng/ul) (Addgene plasmid#139402) and H2B-Halo (100ng/ul) (this paper) was injected into individual blastomeres at the 2-cell stage. Embryos were screened to confirm expression, enabling visualization of cell boundaries and nuclei for lineage tracing. Only morphologically normal embryos were included in downstream analyses. Heterochronic chimeras were generated by aggregating embryos of different maternal ages at the 8-cell stage. Embryos were collected at the 8-cell stage and the zona pellucida was removed by brief incubation in acidic Tyrode's solution, followed by extensive washing in embryo culture medium. For chimera formation, blastomeres from labeled embryos (expressing membrane GFP and H2B-Halo) were combined with unlabeled host embryos. Fusion of embryos was facilitated by close apposition in microwells and confirmed by the formation of a single, re-compacted morula. Aggregates were cultured in KSOM under standard conditions and allowed to recompact and develop to the blastocyst stage. Chimeric embryos were imaged at the blastocyst stage and fixed for immunofluorescence analysis. Lineage identity was assessed using established markers for inner cell mass (ICM; e.g., SOX2) and trophectoderm (TE; e.g., CDX2). The contribution of labeled cells to each lineage was quantified by scoring the proportion of labeled nuclei within ICM Sox2 positive or TE Cdx2 positive compartments.

Cloning IVT vectors and mRNA preparation

The Mammalian Toolkit system was used to construct T7-H2B-Halo via Golden Gate Assembly. In brief, cDNA sequences containing T7, human globulin HBA 3' and 5' UTR, H2B, and Halo were purchased from Twist as gene blocks and constructed using BsaI and T4 Ligase Golden Gate assembly. In vitro transcription was with the mMessage mMachine T3 kit (Thermo Fisher, AM1348). mRNAs were purified using the Monarch Nucleic Acid Purification RNA Cleanup Kit (New England Biolabs Cat#T2040L).

Calculating Trophectoderm Spreading

To analyze trophectoderm spreading, the 650-FastAct channel was used. Only the plane of tissue-substrate adhesion was used to calculate spread area. 650-FastAct was then thresholded in ImageJ to generate an actin mask and then particle analyzed to generate distinct Regions of Interest for each timepoint. ROIs were then measured in ImageJ and values were exported to Excel. The start of implantation was marked as T0 with the appearance of protrusive cells that made a stable blastocyst-substrate attachment that then expanded into an outgrowth. To calculate contact angles during Trophectoderm spreading, z-stacks were resliced in FIJI using the reslice tool, after which they were measured using the angle tool. Embryos were measured for multiple contact angles in 2 cross sections to generate an average contact angle for the embryo as it implants.

Micropipette Aspiration Assay and Analysis

Micropipette Aspiration Package with −69mbar settings (Fluigent Cat#E-MASPI01) was mounted on a Leica DMi8 manual microscope with Integrated Modulation Contrast and Phase Contrast. Imaging was performed using a 40x HI Plan objective with 0.5 Numerical Aperture. Images were acquired using Leica Software at 0.2 millisecond intervals. Pressure was calibrated by using small 10nM spherical silica beads (a kind gift from Zev Gartner's lab) that was mixed with a KSOM microbubble sitting immediately next to the measurement microbubble containing the embryos. Some particle beads were moved into the measurement bubble and zero pressure was calculated based on the point where there was no flow of the beads inwards or outwards of the micropipette. Using a glass micropipette with defined Radius R_p, we non-invasively applied a pressure P_c to cells that exhibit a curvature of $1/R_c$. Micropipette glass (Biomedical Instruments) with diameters of 12μm and 14μm were used for compacting 8-cell stage embryos and E4.5 Blastocysts, respectively. Blastocysts were excluded from analysis if the experimental blastocyst deflated before measurements could be completed. Pressure values were recorded using Fluigent's Oxygen software in parallel with live imaging recordings from the Leica software to match pressure values with cell aspiration. Using FIJI, we manually drew a circle around the target cell or trophectoderm region to analyze the radius of curvature. We used the linescan function to draw a line of the aspirated material into the micropipette to calculate Rp. Using the Young-Laplace equation, we quantified cellular surface tension γ_{cm} before and after the onset of compaction at the 8-cell stage. We then used Excel to calculate surface tension values after Pc was extracted from the Oxygen recordings.

Calculating Compaction Metrics

For initial measurements of developmental tempo, embryos were imaged using either the spinning disk confocal or light sheet microscope. We then calculated developmental tempo as the dwell time within each cell cycle for each embryo. Namely, the timepoint between the resolution of cell division from the previous cell cycle and the initiation of the next subsequent cell division. Cell division was assessed based on the early bulging of the constituent cell and resolution of division or furrow ingression. Timepoints within the timelapse acquisition was marked in Excel and then calculated for dwell timing. To assess compaction metrics' predictive power, embryos were indexed by plating individual embryos in a single square within 155μm Nylon Mesh Filters (Tisch Scientific Cat#ME17300) that were immobilized via Silicone sealant (Rutland Cat#76) on a Glass bottom 35mm Petri Dish with No. 1.5 coverglass (MatTek Cat#P35G1514). Developmental tempo was similarly assayed as above, in addition to measuring blastomere contact angles. At the start and endpoint of the cell cycle, angles between multiple blastomeres were measured in a single plane in Fiji using the angle tool. Multiple angles were then averaged to yield the average embryonic contact angle for the entire embryo to reflect its mechanical state.

Live Imaging

For In Vitro Implantation Assays, E3.5 embryos were denuded with Acidic Tyrode's solution and cultured in IVC media with 1:3000 dilution of 650-FastAct (Cytoskeleton Cat#CY-SC505). Upon imaging implantation, embryos were transferred to fresh IVC including fresh 650-FastAct dilution for subsequent imaging. For imaging preimplantation morphokinetics, embryos were collected at E1.5 and cultured in KSOM-AA and 1:3000 dilution 650-FastAct for direct downstream imaging. Imaging was begun after 4 hours to enable uptake of the 650-FastAct into cytoskeletal structures. Alternatively, embryos were labeled using microinjection technique. mRNA from the vector pRN3P_membrane_EGFP (Addgene Cat#139402) was isolated using mMESSAGE mMACHINE T7 Transcription Kit (ThermoFisher Cat#AM1344) according to manufacturers specifications. Membrane_EGFP RNA was injected at E1.5 into each blastomere of the embryo at concentrations of 100ng/uL. Embryos were placed in an equilibrated and heated droplet of KSOM-AA on a depression slide covered by light mineral oil. Injections were performed using the Eppendorf Femtojet microinjector mounted on Leica DMi8 manual microscope with Integrated Modulation Contrast using a 40x HI Plan objective with 0.5 Numerical Aperture.

Traction Force Microscopy

Traction force microscopy was performed as described previously[49,50]. Briefly, either 25mm round glass coverslips (Electron Microscopy Sciences Cat#72223-01) or 18mm round glass coverslips (Fisher Scientific, Cat#12541005) were cleaned with plasma for 2 minutes using a Plasma Cleaner (Harrick Plasma, Cat#PDC-001). Glass coverslips were then bathed in 2% 3-aminopropyltrimethoxysilane (Sigma Aldrich cat#281778) in isopropanol for 10 minutes, washed 4x for 10 minutes in ddH2O, and then dried overnight covered in tinfoil in a dust-free environment. Coverslips were then treated with 1% glutaraldehyde in ddH2O for 30 minutes, washed 3x for 10 minutes in ddH2O, and again dried overnight in tinfoil a dust-free environment. PAA gel was prepared using a

16kPa Shear modulus Standard Solution with a final working solution of 12% Acrylamide (BioRad Cat#161-0140) and 0.15% Bis-Acrylamide (Fisher Scientific Cat#BP1404-250) and polymerized using 10% Ammonium Persulfate (Fisher Scientific Cat#BP179-25) and TEMED (Fisher Scientific Cat#BPP150-20). Traction Force Microscopy gels additionally contained 200nm fluorescence microspheres (Invitrogen Cat#F8807 or Cat#F8811). Collagen ECM-coupling to the PAA gel was achieved by UV crosslinking of Sulfo-SANPAH (Fisher Scientific Cat#PI22589) diluted in DMSO and incubation with 2mg/mL Collagen (Corning Cat#354236) overnight in $4\degree$C. Gels were rinsed 5-10x in sterile PBS and UV irradiated in a germicidal lamp for 10 minutes before embryo plating in equilibrated IVC media. Embryos were plated onto the gels at E4.5 and imaged prior to implantation attachment to establish baseline reference images of the fluorescent beads. Embryos were pooled by maternal condition and placed in separate wells of the Chamlide, or when both conditions were pooled together, Young embryos were injected at the 2-cell stage with membrane-eGFP and identified post-imaging to denote maternal condition. Traction forces were analyzed using code written in Python (https://github.com/OakesLab/TFM) according to previously described work[70]. Prior to image processing, images were flat-field corrected, with the reference bead image aligned to embryo-attached bead images. Bead displacement was calculated using an optical flow algorithm in OpenCV (Open Source Computer Vision Library, https://github/itseez/opencv) with a window size of 8 pixels. Traction stresses were calculated using the Fourier Transform Traction Cytometry approach[71] with a regularization parameter of 3.35 × 10−6. The total contractile work, or strain energy, was calculated as one half the dot product of the traction stress and displacement vectors, summed over the area of the trophectoderm.

Fit to experimental data

We fit the model solutions (see Supplementary Note) to the experimental data on the evolution of the projected area of the blastocysts, $A(t)$ (Supp. Fig. 2e). By numerically solving [eq:radius_dynamics] and [eq:angle_dynamics] in the Supplementary note, we obtain the radius evolution $R(t)$, from which we obtain $A\left(t\right) = \pi R^2$. We fit this quantity to the experimental data, with the initial contact angle θ_0, the traction magnitude T_0, and the tissue viscosity η as fitting parameters. We estimate the remaining parameters directly from our experimental results. First, we obtain the initial radius R_0 directly from the area measurements as $R_0 = \sqrt{A(t=0)/\pi}$. Second, we use the values of the tissue surface tension measured by micropipette aspiration (Fig. 3c), which are $\gamma_{\mathrm{young}} = 1.4 \pm 0.1$ mN/m and $\gamma_{\mathrm{aged}} = 2.1 \pm 0.1$ mN/m. Third, we estimate the traction decay length L_{c} as follows: The large fluctuations of the experimental traction fields make it difficult to reliably fit the measurements with the model. Consequently, to estimate L_{c}, we locate the minimum (most negative) radial traction near the blastocyst boundary, T_{min}, and we obtain L_{c} as the distance inward at which traction decreases to T_{min}/e (Supp. Fig. 2c). Using this method, we obtain the values shown in Supp. Fig. 2c for embryos from young and aged mothers. Based on these results, we set $L_{\mathrm{c}} = 15\mu$m. This choice reflects a compromise: Rather than discarding the higher values in the long tail of the distribution, we select the upper quartile as a more representative estimate than the median. With these parameter estimates, we obtain fits such

as shown in the examples (Supp. Fig. 2e). From them, we obtain values of the initial contact angle θ_0, which agree well with the experimentally measured contact angles at the moment of attachment (T0 in Supp. Figs. 2d, 2e). We also obtain the average values of the active traction magnitude T_0 and the tissue viscosity η shown in Fig. 3g,h. From the averages, we excluded outliers using an interquartile range (IQR) criterion.

Microscopy

A spinning disk confocal was equipped with a Nikon Ti2-E body and configured with a CrestOptics X-Light V3 confocal spinning disk system, a Lumencor Celesta light engine, Nikon 10x CFI Plan Apo Lambda objective, an Okobox temperature and CO_2 controlled environment, and a Photometrics Kinetix sCMOS camera. Light sheet imaging utilized a Luxendo TruLive3D microscope equipped with a Nikon 25x 1.1NA detection objective and Hamamatsu Flash 4 cameras with a final magnification of 31.25x. Excitation was performed with Omicon and OBIS lasers with an effective light sheet FWHM of 1.6um thick. Human blastocysts were imaged using a confocal Zeiss LSM 700 microscope with the following objective: 20x/0.8 Plan Apo. All images were acquired using LuxBundle software version 4.3.4 and analyzed in FIJI.

Embryoscope data and analysis

Embryoscope time-lapse data were de-identified and exported from the Fertility Clinic at Northwestern University's Center for Reproductive Science under a protocol approved by the institutional review board. All exports were performed by clinical staff not involved in downstream analysis. Prior to transfer, each embryo's dataset (including image sequences, metadata, and developmental annotations) was de-identified at the source. Patient identifiers (e.g., name, date of birth, medical record number), cycle identifiers, treatment dates, and any clinic-specific information were removed automatically through the laboratory's standard Embryoscope export workflow. Each embryo was then assigned a random, non-derivable study ID generated by the clinical team. Study IDs encoded no clinical, temporal, or biological information. The corresponding key linking original identifiers to study IDs was retained exclusively by the clinical laboratory and was not accessible to research personnel. All image files were inspected upon receipt to confirm that embedded metadata (file headers, timestamps, and annotation layers) contained no residual identifiable information. De-identified datasets were stored on encrypted institutional servers and accessed only by authorized research staff under IRB oversight.

Embryos were binned based on maternal age and pregnancy outcome. Group 1, or "Young" embryos, consisted of embryos donated from women <28 years of age and transferred to aged recipients >40 years of age. Group 1 embryos also displayed successful pregnancy and full-term births post uterine transfer. Ploidy status was not indicated for these embryos, as they displayed successful live births post-transfer. Group 2, or "Aged" embryos, consisted of embryos retrieved from women >40 years of age and transferred to aged recipients >40 years of age. Group 2 embryos were all of euploid genetic status and displayed a failure in implantation with no live births.

Time to initial compaction was measured from time-lapse images acquired using the Embryoscope system. Compaction was defined operationally as the first frame in which individual blastomeres could no longer be distinguished by clear cell–cell borders. Prior to this point, blastomeres exhibit sharp, optically distinct junctions and discrete intercellular interfaces. The onset of compaction was annotated when these interfaces progressively disappeared, resulting in a continuous, smooth outer surface and loss of visible boundaries between adjacent cells. Time to initial compaction was calculated as the elapsed time between the start of the 8-cell stage and the annotated frame marking the disappearance of blastomere junctions. All timelapses were blinded to maternal age and clinical outcome. Embryonic data were excluded if constituent embryos were too fragmented to display cell-cell junctions, thus making compaction difficult to assay clearly. At the start of the 8-cell stage and time of initial compaction, angles between multiple blastomeres were measured in a single plane in Fiji using the angle tool. Multiple angles were then averaged to yield the average embryonic contact angle for the entire embryo to reflect its mechanical state.

Statistical Analysis

Statistical analysis was performed in Excel, GraphPad Prism, and Matlab, to establish statistical significance under the defined specific experimental conditions. Outliers were identified using the ROUT method (Robust regression and outlier removal) with a false discovery rate of Q=5% and excluded from subsequent analysis. The statistical test used, exact n values, and definition of replicates are provided in the figure legends. N represents the experimental replicates, and n represents the number of embryos used in the indicated maternal or drug conditions. Data were analyzed for significance with ****=$p<0.0001$, ***=$p<0.001$, **=$p<0.01$, and *=$p<0.05$, which is indicated in the figure and its respective legend, as determined by respective tests described in the figure legends. No statistical methods were used to pre-determine sample sizes but our sample sizes are similar to those reported in previous publications (refs 26, 27, 28, 29, 30, 31). Statistical analyses were performed using non-parametric tests where appropriate. Data distributions were not assumed to be Gaussian, and formal tests of normality were not performed. Comparisons between two groups were conducted using two-sided Mann–Whitney U tests. Individual data points are shown in all plots whenever possible. Animals were assigned to experimental groups on the basis of age, which constituted the primary experimental variable. Therefore, animals were not randomly allocated to young and aged groups. Embryos were collected and analyzed from the designated age groups under identical experimental conditions. No randomization was applied to the organization of experimental conditions or stimulus presentation. Investigators were blinded to group allocation during analysis of human Embryoscope datasets and during focal adhesion segmentation and quantification. For most mouse embryo experiments, blinding was not feasible during data collection because experimental groups were defined by maternal age or pharmacological treatment and embryos were cultured, processed, and imaged under condition-specific experimental workflows. Quantitative image analysis was performed using predefined analysis pipelines and objective measurement criteria. No samples were excluded on the basis of experimental outcome.

Extended Data

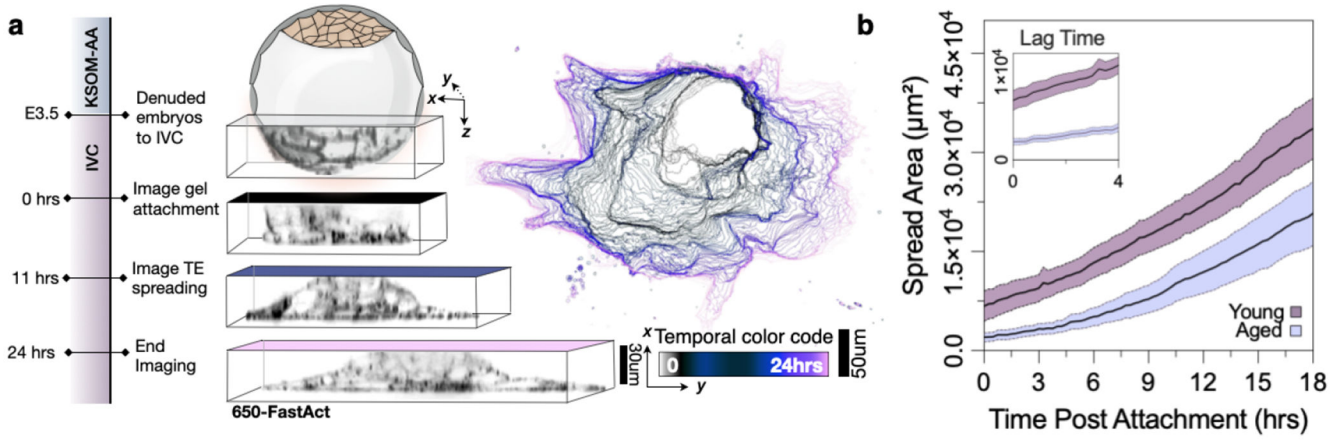

Extended Data Figure 1. In vitro assays reveal dynamics of spreading during implantation.

a) Diagram showing the experimental workflow for In Vitro Implantation Assays. E3.5 Blastocysts are denuded and transferred from KSOM-AA to IVC media that contained 650-FastAct to visualize the process of implantation on collagen-coated polyacrylamide gels. 24 hours post-implantation, the embryos are fixed (left). Views of the blastocyst in Z show mural Trophectoderm attachment, blastocyst cavity collapse, and spreading over the 24 hours post-implantation (middle). Mural Trophectoderm perimeter outlines show the evolution of mTE spreading over 24 hours. Perimeter outlines are color coded based on time post-implantation (right). Scale bars are 30µm and 50µm, as indicated. b) Graph of the evolution of the Trophectoderm's spread area over 24 hours of implantation. Inlay shows a zoom of the first 4 hours of implantation, displaying an age-specific delay in attachment and spreading (Young N = 5, n = 26 implanting blastocysts; Aged N = 4, n = 31 implanting blastocysts). Lines and shading show mean and 95 percent confidence interval.

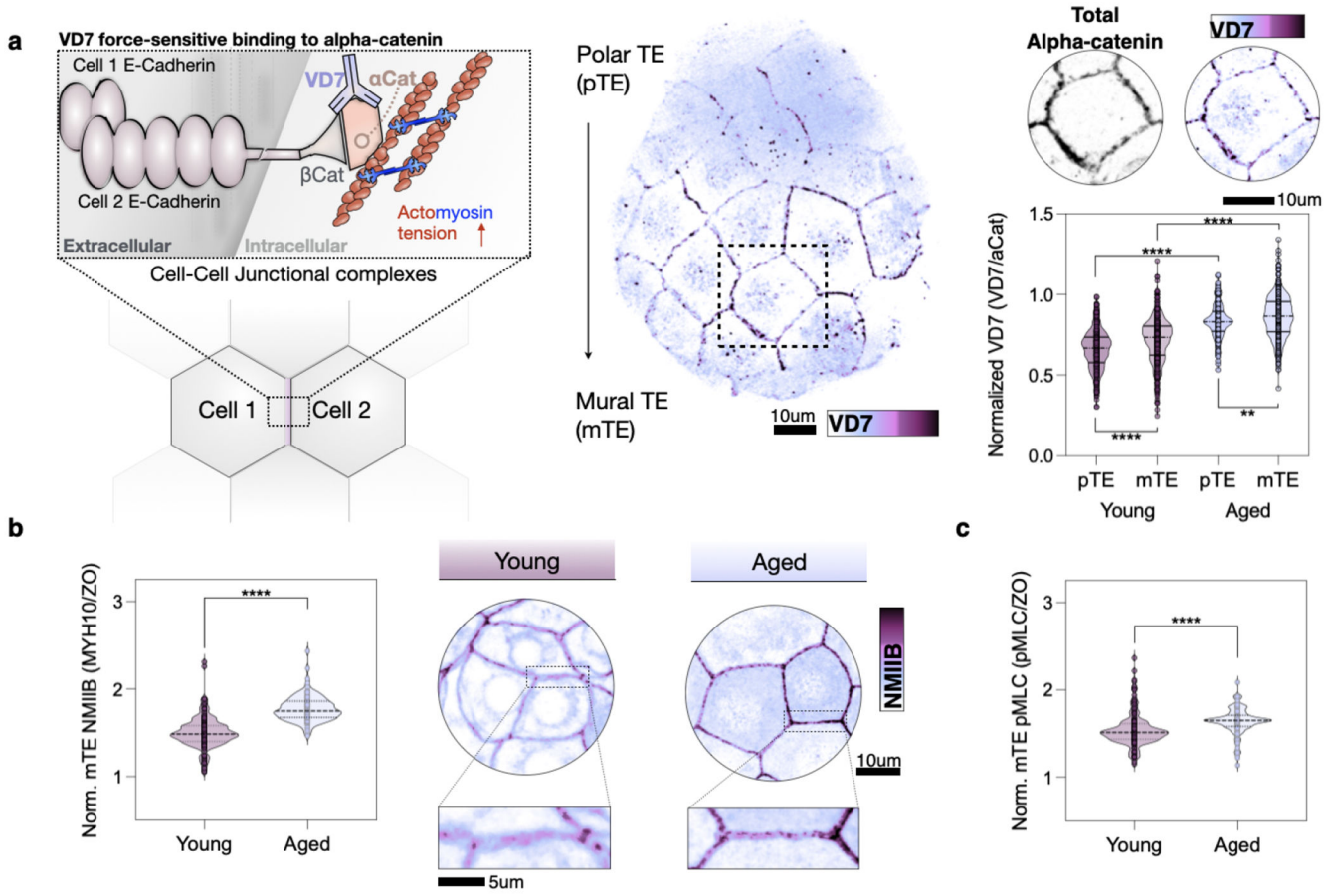

Extended Data Figure 2. Maternally aged embryos show increased mechanochemical signaling .

a) Immunostaining of late E4.5 blastocysts with the tension sensor, VD7. The VD7 antibody is an engineered antibody sequence based on vinculin's binding association to alpha-catenin. Contractility at cell-cell junctions creates a force-dependent conformational change in alpha-catenin proteins that exposes this epitope pocket to which vinculin binds. VD7 association is observed when E-cadherinmediated adhesions experience tension, making it an indicator of tissue under tensile strain. We measured global junctional VD7 and normalized its levels to total alpha catenin to quantify relative junctional VD7 signal intensity. Blastocyst fixed and stained for tension sensor VD7, showing increasing junctional VD7 towards the mural trophectoderm region. Normalized VD7 (purple) was calculated over total alpha-catenin (black), showing that maternally aged embryos show higher junctional tensions both at the mural and polar trophectoderm regions. (Young N = 4, n = 386 pTE junctions, 532 mTE junctions, 10 blastocysts; Aged N = 3, n = 218 pTE junctions, 383 mTE junctions, 8 blastocysts). p values from Mann-Whitney test. Scale bar is 10μm. b) Plot showing Normalized junctional NMIIB staining in the mTE region, with higher junctional accumulation in the aged condition (left) (Young N = 2, n = 1,610 mTE junctions, 17 blastocysts; Aged N = 2, n = 935 mTE junctions, 14 blastocysts). p values from Mann-Whitney test. Scale bar is 10μm. Representative images of NMIIB staining (purple) in both maternal conditions. Scale bar is 5μm and 10μm. c) Plot showing Normalized junction pMLC staining in the mTE region, with higher junctional accumulation in the aged

condition (Young N = 2, n = 1,610 mTE junctions, 17 blastocysts; Aged N = 2, n = 935 mTE junctions, 14 blastocysts). p values from Mann-Whitney test.

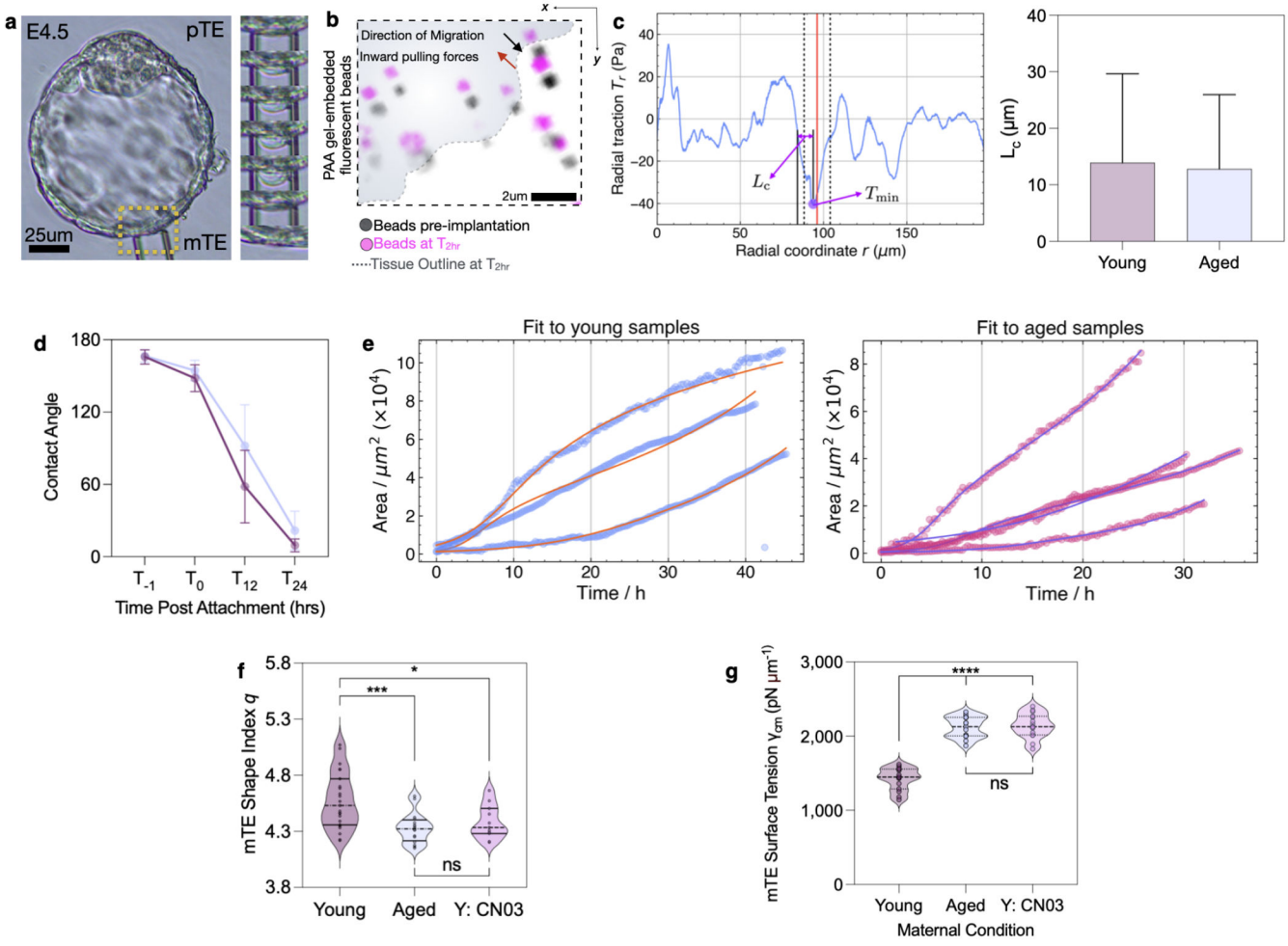

Extended Data Figure 3. Aged embryos show increased viscosity in the wetting model.

a) Representative image of an E4.5 aged blastocyst undergoing Micropipette aspiration assay at the mural trophectoderm region (left) with zoomed-in timelapse of the yellow highlighted region showing the progression of tissue aspiration over time (right). Scale bar is 25μm. b) Representative outline of a migrating trophectoderm front (shaded blue) in the direction of the black arrow, with pulling forces going in the opposite direction. Black beads represent the reference image of the beads before implantation, with the pink beads representing the beads after 2 hours of implantation, together showing bead displacement as a function of tissue migration. Scale bar is 2μm. c) Example frame of a radial traction profile used to estimate Lc. The red line marks the blastocyst boundary, while the dashed lines indicate the window around the boundary used to account for uncertainties in image analysis. Within this window, the minimum traction is identified, and Lc is determined as the distance at which the traction decays to T0/e (left). Measurements of the length scale Lc extracted from the traction stress profiles (Young n = 589 profiles; Aged n = 642 profiles). Box plots show mean and SD (right). d) Measurement of blastocyst contact angles over 24 hours of

implantation (Young N = 3, n = 41 blastocysts; Aged N = 3, n = 41 blastocysts). Dots represent mean with SD. e) Example of model fits to the blastocyst area expansion for both maternal conditions. Colored dots represent the area measurements. Solid lines indicate the model fits. f) Plot showing individual q values for cells in the mTE region of blastocysts from Young, Aged, and Young-CN03 treated embryos (Young N = 3, n = 384 cells, 27 Blastocysts; Aged N = 3, n = 239 cells, 19 Blastocysts; Young-CN03 N = 3, n = 221 cells, 22 Blastocysts). p values from Mann-Whitney test. g) Plot showing surface tension measurements of E4.5 blastocysts from Young, Aged, and Young-CN03 treated embryos (Young N = 3, n = 15 blastocysts; Aged N = 3, n = 15 blastocysts; Young-CN03 N = 3, n = 15 blastocysts). p values from Mann-Whitney test.

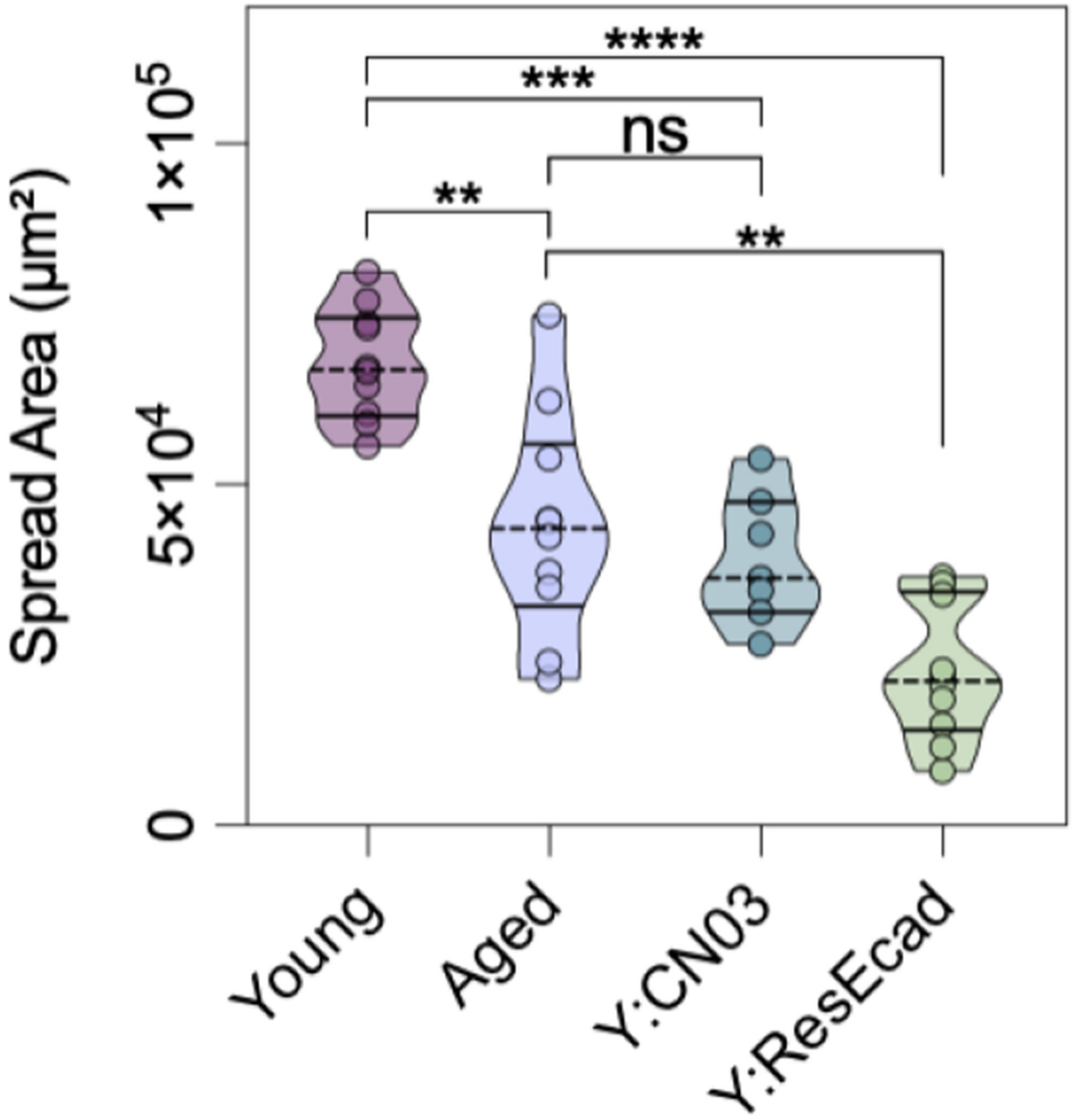

Extended Data Figure 4. Increasing tissue viscosity recapitulates the aged phenotype.

Plot showing final spread area for Young, Aged, CN03, and ResEcad treatment (Young N = 9, n = 63 implanting blastocysts; Aged N = 4, n = 27 implanting blastocysts; Young-CN03 N = 5, n = 25 implanting blastocysts; Young-ResEcad N = 2, 17 implanting blastosysts). ResEcad treated Young embryos show significant reduction in final spread area. p values from Mann-Whitney test.

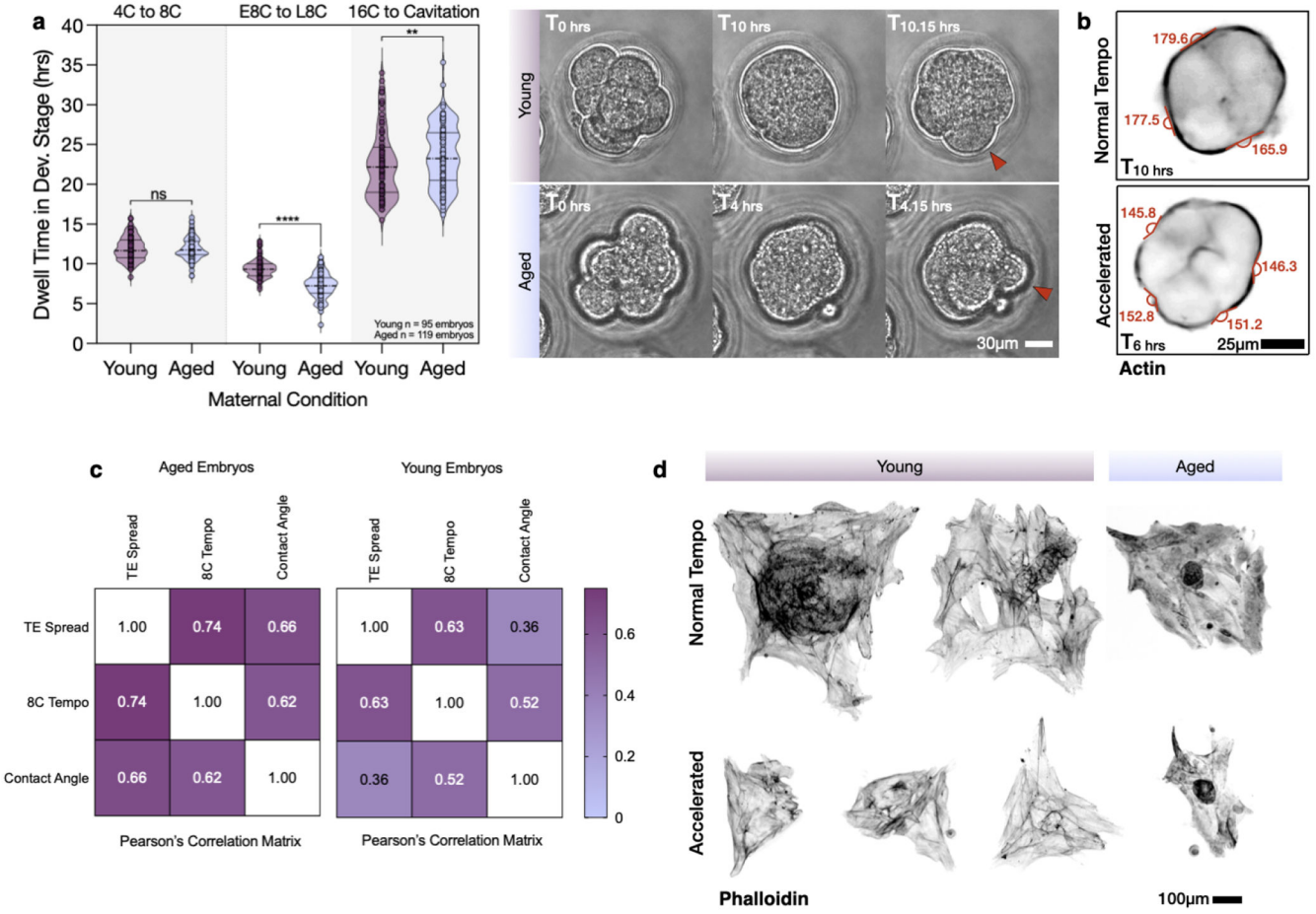

Extended Data Figure 5. Compaction metrics predict implantation potential.

a) Quantification of developmental tempo for all examined stages. Compaction undergoes an age-related abbreviation, while cavitation timing is lengthened (left) (N=4, Young n = 95 embryos; Aged n = 119 embryos). p values from Mann-Whitney test. Timelapse video (right) showing Young (top) and Aged (bottom) embryos undergoing compaction using Brightfield imaging. T0 marks the beginning of the 8-cell stage. Aged embryo undergoes a significantly accelerated compaction from the early to late 8-cell stage. Red arrows denote cell divisions, denoting the end of the 8-cell stage. Scale bar is 30µm. b) Representative images from a timelapse of embryos stained for 650-FastAct showing Normal and Accelerated compaction conditions. Red labels denote the calculated inter blastomere contact angles. Accelerated compacted embryos showed more acute angles than embryos with Normal tempo. Scale bar is 25µm. c) Pearson's correlation matrix showing correlation between final trophectoderm spreading, 8-cell compaction tempo, and final compaction inter-blastomere contact angles for both maternal conditions. Both 8-cell tempo and contact angles show significant correlations to final trophectoderm spreading values (Young n=56 embryos; Aged n = 14 embryos). d) Representative images of implanted embryos stained for Actin that underwent Normal (top) and Accelerated (bottom) compaction rates. Aged embryos are denoted with light purple color. Embryos selected for normal compaction tempo exhibited robust trophectoderm spreading events in both

maternal conditions. Embryos selected for accelerated compaction tempos showed reduced trophectoderm spreading in both conditions. Scale bar is 100μm.

Supplementary Material

Refer to Web version on PubMed Central for supplementary material.

Acknowledgements:

We thank the entire Weiner Lab for helpful suggestions insightful comments, and critical reading of the text. We thank Sneha Rao and Elysse Phillips of the Weiner Lab with critical help setting up the mouse embryo as the model system of use, in addition to setting up experimental frameworks. We thank Dane Maxfield (Bruker) for generous use of the TruLive3D Lightsheet Microscope. We thank UCSF's Center for Advanced Light Microscopy (CALM) for use of its core microscopes.

Funding Statement:

KEC was supported by Jane Coffin Childs Postdoctoral Fellowship, Burroughs Wellcome Fund Postdoctoral Enrichment Program, Bakar Aging Research Institute Postdoctoral Fellowship, and Burroughs Wellcome Fund Career Award at the Scientific Interface. ODW was supported by GM118167, a Sandler Program for Breakthrough Biomedical Research Grant, and a collaborative grant with Altos. FED and MP was supported by the Thomas J. Watkins Memorial Endowment (FED) and Northwestern Departmental Startup Funds (FED). NH was supported by the Blavatnik Fellowship and CIRM Graduate Research Fellowship. MM was supported by the Stanford Dunlevie Maternal Fetal Medicine Center for Discovery, Innovation and Impact, the Duan Family Faculty Scholar in Maternal-Fetal Medicine, the FY25 ASRM Discovery & Innovation Grant from the American Society for Reproductive Medicine, the California Institute for Regenerative Medicine (Grant DISC0–17685). PO was supported by GM148644. DJL was supported by 1R01GM122902, 1R01ES023297, and the Global Consortium for Reproductive Health through the Bia-Echo Foundation GCRLE-0123. MJFO and RA acknowledge funding from the Max Planck Society. RA acknowledges funding from the European Union's ERC Starting Grant "Living Fluctuations" No. 101114584. The funders had no role in study design, data collection and analysis, decision to publish or preparation of the manuscript.

Data Availability

Previously published Surrogacy data was collated from the Human Fertilisation and Embryology Authority (HFEA) [24]. cDNA sequences were obtained from NCBI and DNA maps from Addgene cDNA sequences containing T7 (Addgene Plasmid #156454), human globulin HBA 3' and 5' UTR (accession #NM_000558), H2B (Addgene Plasmid #11680), and Halo (Addgene Plasmid #112850). All data supporting the findings of this study are available from the corresponding author upon reasonable request. The raw live-imaging and microscopy datasets generated during the current study are several terabytes in size and therefore cannot be readily hosted in a public repository. Processed data underlying all figures and analyses are available from the corresponding author upon request. Numerical source data are provided with this study.

Code Availability

Traction forces were analyzed using code written in Python (https://github.com/OakesLab/TFM) according to previously described work [70]. Bead displacement was calculated using an optical flow algorithm in OpenCV (Open Source Computer Vision Library https://github.com/opencv/opencv)

References

1. Larsen EC, Christiansen OB, Kolte AM & Macklon N. New insights into mechanisms behind miscarriage. BMC Med 11, 154 (2013). [PubMed: 23803387]
2. Bashiri A, Halper KI & Orvieto R. Recurrent Implantation Failure-update overview on etiology, diagnosis, treatment and future directions. Reproductive Biology and Endocrinology 16, 121 (2018). [PubMed: 30518389]
3. Broekmans FJ, Soules MR & Fauser BC. Ovarian Aging: Mechanisms and Clinical Consequences. Endocrine Reviews 30, 465–493 (2009). [PubMed: 19589949]
4. Zhang J-J et al. Advanced maternal age alters expression of maternal effect genes that are essential for human oocyte quality. Aging 12, 3950–3961 (2020). [PubMed: 32096767]
5. Amargant F et al. Ovarian stiffness increases with age in the mammalian ovary and depends on collagen and hyaluronan matrices. Aging Cell 19, e13259 (2020). [PubMed: 33079460]
6. Shapiro BS et al. The risk of embryo-endometrium asynchrony increases with maternal age after ovarian stimulation and IVF. Reproductive BioMedicine Online 33, 50–55 (2016). [PubMed: 27178763]
7. Braude P & Flinter F. Use and misuse of preimplantation genetic testing. BMJ 335, 752–754 (2007). [PubMed: 17823145]
8. Nikalayevich E et al. Aberrant cortex contractions impact mammalian oocyte quality. Developmental Cell 59, 841–852.e7 (2024). [PubMed: 38387459]
9. Bennabi I et al. Artificially decreasing cortical tension generates aneuploidy in mouse oocytes. Nat Commun 11, 1649 (2020). [PubMed: 32245998]
10. Strieby A, McCallie BR, Parks JC, Schoolcraft WB & Katz-Jaffe MG. Blastocysts from women of advanced maternal age have compromised transcription of key implantation and development genes. Fertility and Sterility 102, e20 (2014).
11. Chen Z et al. Advanced maternal age causes premature placental senescence and malformation via dysregulated α-Klotho expression in trophoblasts. Aging Cell 20, e13417 (2021). [PubMed: 34105233]
12. Torous VF & Roberts DJ. Placentas From Women of Advanced Maternal Age: An Independent Indication for Pathologic Examination? Archives of Pathology & Laboratory Medicine 144, 1254–1261 (2020). [PubMed: 32101452]
13. Napso T, Hung Y-P, Davidge ST, Care AS & Sferruzzi-Perri AN. Advanced maternal age compromises fetal growth and induces sex-specific changes in placental phenotype in rats. Sci Rep 9, 16916 (2019). [PubMed: 31780670]
14. Ly KD, Agarwal A & Nagy ZP. Preimplantation genetic screening: does it help or hinder IVF treatment and what is the role of the embryo? J Assist Reprod Genet 28, 833–849 (2011). [PubMed: 21743973]
15. Chen M, Wei S, Hu J, Yuan J & Liu F. Does time-lapse imaging have favorable results for embryo incubation and selection compared with conventional methods in clinical in vitro fertilization? A meta-analysis and systematic review of randomized controlled trials. PLOS ONE 12, e0178720 (2017). [PubMed: 28570713]
16. Chera-aree P, Thanaboonyawat I, Thokha B & Laokirkkiat P. Comparison of pregnancy outcomes using a time-lapse monitoring system for embryo incubation versus a conventional incubator in in vitro fertilization: An age-stratification analysis. Clin Exp Reprod Med 48, 174–183 (2021). [PubMed: 34024081]
17. Fragouli E et al. Analysis of implantation and ongoing pregnancy rates following the transfer of mosaic diploid-aneuploid blastocysts. Hum Genet 136, 805–819 (2017). [PubMed: 28393271]
18. Londero AP, Rossetti E, Pittini C, Cagnacci A & Driul L. Maternal age and the risk of adverse pregnancy outcomes: a retrospective cohort study. BMC Pregnancy and Childbirth 19, 261 (2019). [PubMed: 31337350]
19. Heazell AEP, Newman L, Lean SC & Jones RL. Pregnancy outcome in mothers over the age of 35. Current Opinion in Obstetrics and Gynecology 30, 337–343 (2018). [PubMed: 30239372]

20. Nasiri N & Eftekhari-Yazdi P. An Overview of The Available Methods for Morphological Scoring of Pre-Implantation Embryos in In Vitro Fertilization. Cell J 16, 392–405 (2015). [PubMed: 25685730]
21. Viotti M et al. Using outcome data from one thousand mosaic embryo transfers to formulate an embryo ranking system for clinical use. Fertility and Sterility 115, 1212–1224 (2021). [PubMed: 33685629]
22. Gleicher N et al. A single trophectoderm biopsy at blastocyst stage is mathematically unable to determine embryo ploidy accurately enough for clinical use. Reproductive Biology and Endocrinology 15, 33 (2017). [PubMed: 28449669]
23. Paulson RJ. Hidden in plain sight: the overstated benefits and underestimated losses of potential implantations associated with advertised PGT-A success rates. Human Reproduction 35, 490–493 (2020). [PubMed: 32100030]
24. HFEA dashboard. Human Fertilisation & Embryology Authority (HFEA) https://www.hfea.gov.uk/about-us/hfea-dashboard/.
25. Domingo-Muelas A et al. Human embryo live imaging reveals nuclear DNA shedding during blastocyst expansion and biopsy. Cell 186, 3166–3181.e18 (2023). [PubMed: 37413989]
26. Zenker J et al. Expanding Actin Rings Zipper the Mouse Embryo for Blastocyst Formation. Cell 173, 776–791.e17 (2018). [PubMed: 29576449]
27. Hernandez B et al. Actin organizes chromosomes and microtubules to ensure mitotic fidelity in the preimplantation embryo. Science 388, eads1234 (2025). [PubMed: 40403077]
28. Skory RM et al. The nuclear lamina couples mechanical forces to cell fate in the preimplantation embryo via actin organization. Nat Commun 14, 3101 (2023). [PubMed: 37248263]
29. Zhu M, Leung CY, Shahbazi MN & Zernicka-Goetz M. Actomyosin polarisation through PLC-PKC triggers symmetry breaking of the mouse embryo. Nat Commun 8, 921 (2017). [PubMed: 29030553]
30. Zhu M et al. Developmental clock and mechanism of de novo polarization of the mouse embryo. Science 370, (2020). [PubMed: 32703862]
31. Zhu M et al. Human embryo polarization requires PLC signaling to mediate trophectoderm specification. eLife 10, e65068 (2021). [PubMed: 34569938]
32. Godeau AL et al. Traction force and mechanosensitivity mediate species-specific implantation patterns in human and mouse embryos. Science Advances 11, eadr5199 (2025). [PubMed: 40815643]
33. Bondarenko V et al. Embryo-uterine interaction coordinates mouse embryogenesis during implantation. The EMBO Journal 42, e113280 (2023). [PubMed: 37522872]
34. Muter J, Lynch VJ, McCoy RC & Brosens JJ. Human embryo implantation. Development 150, dev201507 (2023). [PubMed: 37254877]
35. Weberling A & Zernicka-Goetz M. Trophectoderm mechanics direct epiblast shape upon embryo implantation. Cell Reports 34, (2021).
36. Green MA, Bass S & Spear BT. A device for the simple and rapid transcervical transfer of mouse embryos eliminates the need for surgery and potential post-operative complications. BioTechniques 47, 919–924 (2009). [PubMed: 20041845]
37. Pan H, Ma P, Zhu W & Schultz RM. Age-associated increase in aneuploidy and changes in gene expression in mouse eggs. Developmental Biology 316, 397–407 (2008). [PubMed: 18342300]
38. Duncan FE et al. Age-associated dysregulation of protein metabolism in the mammalian oocyte. Aging Cell 16, 1381–1393 (2017). [PubMed: 28994181]
39. Morris SA, Guo Y & Zernicka-Goetz M. Developmental Plasticity Is Bound by Pluripotency and the Fgf and Wnt Signaling Pathways. Cell Reports 2, 756–765 (2012). [PubMed: 23041313]
40. Bedzhov I & Zernicka-Goetz M. Self-Organizing Properties of Mouse Pluripotent Cells Initiate Morphogenesis upon Implantation. Cell 156, 1032–1044 (2014). [PubMed: 24529478]
41. Pérez-González C et al. Active wetting of epithelial tissues. Nature Phys 15, 79–88 (2019). [PubMed: 31537984]
42. Blauth E et al. Different contractility modes control cell escape from multicellular spheroids and tumor explants. APL Bioeng 8, 026110 (2024). [PubMed: 38721268]

43. Cavanaugh KE et al. Force-dependent intercellular adhesion strengthening underlies asymmetric adherens junction contraction. Current Biology 32, 1986–2000.e5 (2022). [PubMed: 35381185]
44. Okumura N et al. Effect of the Rho-Associated Kinase Inhibitor Eye Drop (Ripasudil) on Corneal Endothelial Wound Healing. Investigative Ophthalmology & Visual Science 57, 1284–1292 (2016). [PubMed: 26998714]
45. Garnock-Jones KP. Ripasudil: First Global Approval. Drugs 74, 2211–2215 (2014). [PubMed: 25414122]
46. Duong CN et al. Force-induced changes of α-catenin conformation stabilize vascular junctions independently of vinculin. J Cell Sci 134, jcs259012 (2021). [PubMed: 34851405]
47. Alert R & Trepat X. Physical Models of Collective Cell Migration. Annual Review of Condensed Matter Physics 11, 77–101 (2020).
48. Pallarès ME et al. Stiffness-dependent active wetting enables optimal collective cell durotaxis. Nat. Phys. 19, 279–289 (2023).
49. Oakes PW, Beckham Y, Stricker J & Gardel ML. Tension is required but not sufficient for focal adhesion maturation without a stress fiber template. Journal of Cell Biology 196, 363–374 (2012). [PubMed: 22291038]
50. Oakes PW, Banerjee S, Marchetti MC & Gardel ML. Geometry Regulates Traction Stresses in Adherent Cells. Biophysical Journal 107, 825–833 (2014). [PubMed: 25140417]
51. Mertz AF et al. Scaling of Traction Forces with the Size of Cohesive Cell Colonies. Phys. Rev. Lett. 108, 198101 (2012). [PubMed: 23003091]
52. Bi D, Yang X, Marchetti MC & Manning ML. Motility-Driven Glass and Jamming Transitions in Biological Tissues. Phys. Rev. X 6, 021011 (2016).
53. Grosser S et al. Cell and Nucleus Shape as an Indicator of Tissue Fluidity in Carcinoma. Phys. Rev. X 11, 011033 (2021).
54. Park J-A et al. Unjamming and cell shape in the asthmatic airway epithelium. Nature Mater 14, 1040–1048 (2015). [PubMed: 26237129]
55. Dumortier JG et al. Hydraulic fracturing and active coarsening position the lumen of the mouse blastocyst. Science 365, 465–468 (2019). [PubMed: 31371608]
56. Chan CJ et al. Hydraulic control of mammalian embryo size and cell fate. Nature 571, 112–116 (2019). [PubMed: 31189957]
57. Maître J-L, Niwayama R, Turlier H, Nédélec F & Hiiragi T. Pulsatile cell-autonomous contractility drives compaction in the mouse embryo. Nature Cell Biology 17, 849–855 (2015). [PubMed: 26075357]
58. Korotkevich E et al. The Apical Domain Is Required and Sufficient for the First Lineage Segregation in the Mouse Embryo. Developmental Cell 40, 235–247.e7 (2017). [PubMed: 28171747]
59. Maître J-L et al. Asymmetric division of contractile domains couples cell positioning and fate specification. Nature 536, 344–348 (2016). [PubMed: 27487217]
60. Niwayama R et al. A Tug-of-War between Cell Shape and Polarity Controls Division Orientation to Ensure Robust Patterning in the Mouse Blastocyst. Developmental Cell 51, 564–574.e6 (2019). [PubMed: 31735668]
61. Yang L et al. Machine learning in time-lapse imaging to differentiate embryos from young vs old mice†. Biology of Reproduction 110, 1115–1124 (2024). [PubMed: 38685607]
62. Firmin J et al. Mechanics of human embryo compaction. Nature 629, 646–651 (2024). [PubMed: 38693259]
63. Yang M et al. Depletion of aneuploid cells in human embryos and gastruloids. Nat Cell Biol 23, 314–321 (2021). [PubMed: 33837289]
64. Zhang S et al. Hippo Signaling Suppresses Cell Ploidy and Tumorigenesis through Skp2. Cancer Cell 31, 669–684.e7 (2017). [PubMed: 28486106]
65. Balough JL, Dipali SS, Velez K, Kumar TR & Duncan FE. Hallmarks of female reproductive aging in physiologic aging mice. Nat Aging 4, 1711–1730 (2024). [PubMed: 39672896]
66. Mara JN et al. Ovulation and ovarian wound healing are impaired with advanced reproductive age. Aging 12, 9686–9713 (2020). [PubMed: 32407290]

67. Mejía-Ramírez E et al. Targeting RhoA activity rejuvenates aged hematopoietic stem cells. 2025.04.23.647902 Preprint at 10.1101/2025.04.23.647902 (2025).

68. Wang H et al. Rejuvenation of aged oocyte through exposure to young follicular microenvironment. Nat Aging 4, 1194–1210 (2024). [PubMed: 39251866]

69. Amargant F, Magalhaes C, Pritchard MT & Duncan FE. Systemic low-dose anti-fibrotic treatment attenuates ovarian aging in the mouse. GeroScience 47, 3475–3495 (2025). [PubMed: 39285140]

70. Schmitt MS et al. Machine learning interpretable models of cell mechanics from protein images. Cell 187, 481–494.e24 (2024). [PubMed: 38194965]

71. Huang Y et al. Traction force microscopy with optimized regularization and automated Bayesian parameter selection for comparing cells. Sci Rep 9, 539 (2019). [PubMed: 30679578]

72. de Gennes PG and Prost J. The Physics of Liquid Crystals. Oxford University PressOxford (1993).

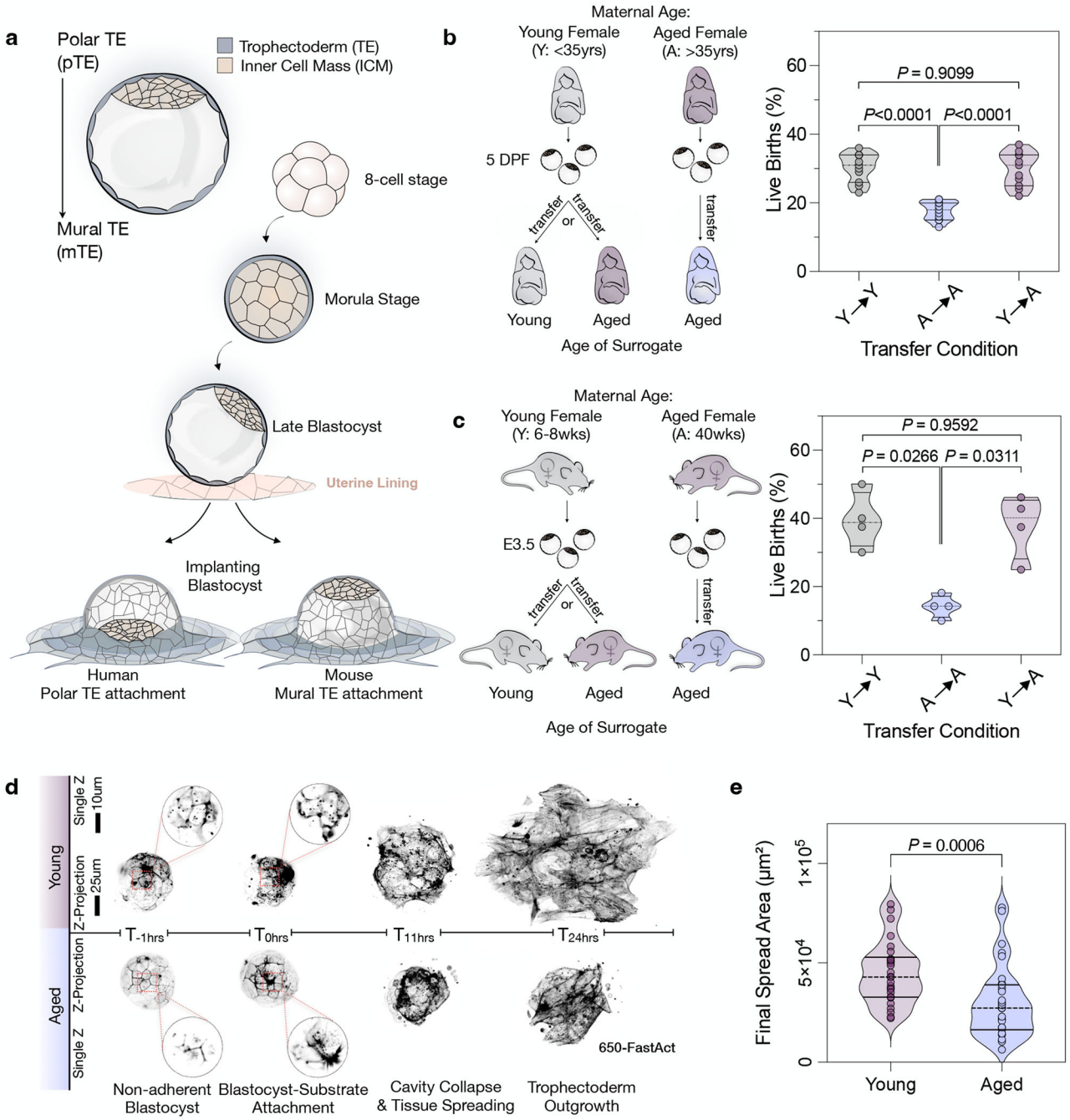

Figure 1: Embryos from aged females exhibit reduced implantation.

a) Schematic of blastocyst structure with the Inner Cell Mass (ICM) (tan) sitting within the blastocyst and surrounded by the Trophectoderm tissue (gray). The ICM sits at the Polar Trophectoderm (pTE) region, with the opposite side being the Mural Trophectoderm (mTE) (top left). Schematic of distinct developmental checkpoints spanning the 8-cell, morula, blastocyst, and implanting blastocyst stage. Species-specific differences occur at the site of implantation: the mouse embryo implants at the mural Trophectoderm (left), whereas the human embryo implants at the polar Trophectoderm (right). **b)** Schematic

of Uterine Transfer workflow in Assisted Reproductive Technologies parsed from the HFEA[24]. Embryos are transferred individually to the uterus. Embryos from Young or Aged females are transferred to either Young or Aged surrogate mothers (Y->Y n = 318,975 transferred embryos; A->A n = 34,255 transferred embryos; Y->A n = 482,730 transferred embryos). Violin plots show a reduction in age-related infertility that is rescued with embryos from younger women following transfer to older surrogates. Two tailed p values from Mann-Whitney test. **c)** Schematic of NSET workflow to simulate Assisted Reproductive Technologies. Embryos from Young or Aged females are transferred to either Young or Aged surrogate mothers (N=4 for all transfer conditions, Y->Y n = 38 transferred embryos; A->A n = 35 transferred embryos; Y->A n = 36 transferred embryos). Violin plots show a reduction in age-related infertility that is rescued with developmentally younger embryos when transferred to older females. Two tailed p values from N-1 Chi-Square test. **d)** Representative images of Young and Aged implanting blastocysts over the 24 hours post-implantation. Blastocysts are initially non-adherent, after which they extend protrusions to mediate attachment, cavity collapse, and tissue spreading. Inlays display a single z-plane to visualize mural Trophectoderm protrusions at the substrate surface. Images of implanting blastocysts are displayed as a z-projection. Scale bars are 10 μm and 25 μm, as indicated. **e)** Violin plot depicted total spread area 24 hours post-implantation for both maternal conditions (Young N = 5, n = 25 implanting blastocysts; Aged N = 4, n = 31 implanting blastocysts). Maternally aged embryos show significant reductions in final spread area. Two tailed p values from Mann-Whitney test.

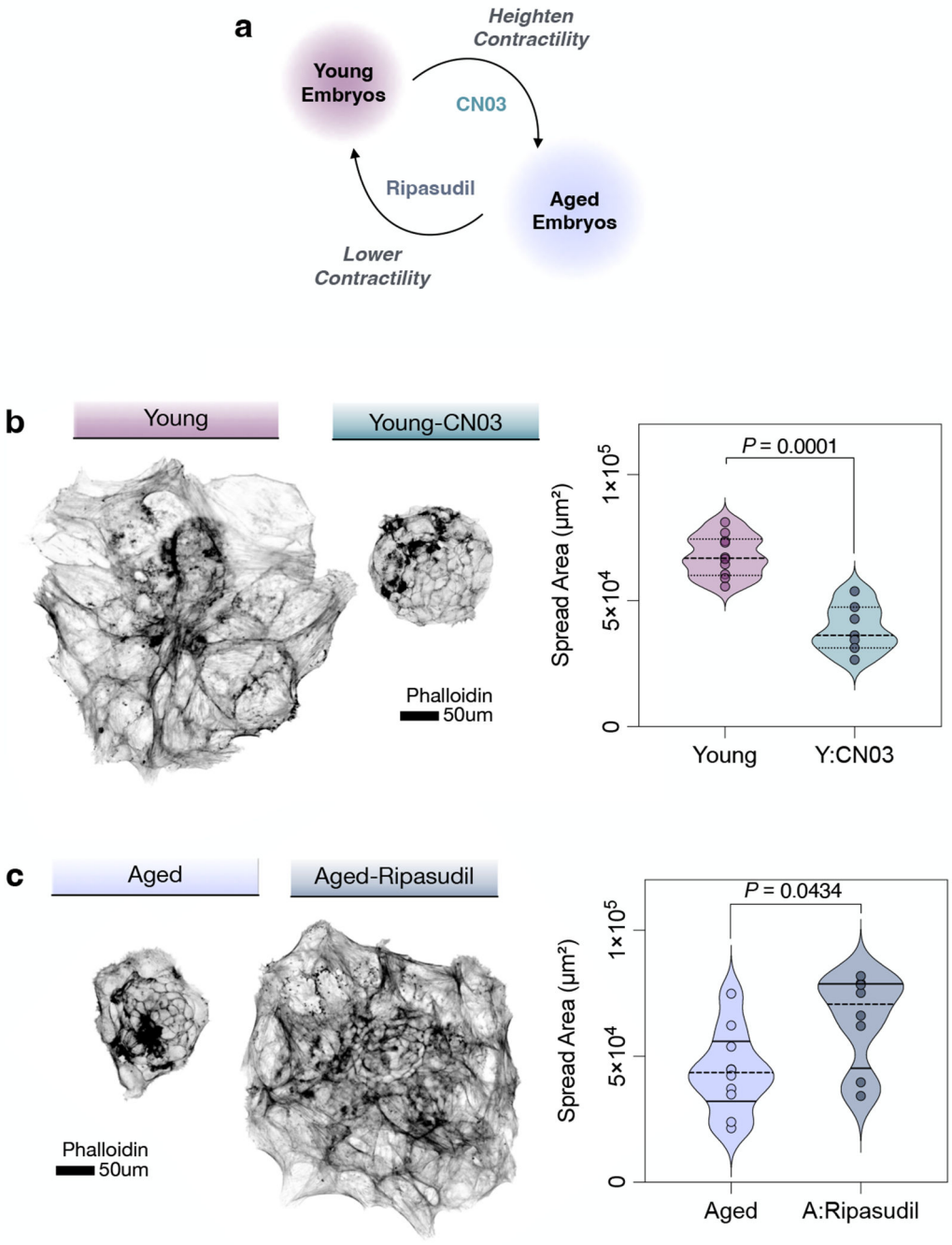

Figure 2: Contractility is necessary and sufficient for maternal age-related implantation defects.

a) Schematic of contractile inhibitor pathways to regulate potential trophectoderm spreading behaviors. We hypothesized that RhoA activator CN03 would phenocopy aged embryos, while ROCK inhibitor Ripasudil would rescue aged spreading behaviors. **b)** Representative images of Young (left) and Young-CN03 treated (right) embryos fixed and stained for actin. Violin plot shows a reduction of spread area in Young-CN03 treated embryos (Young N = 9, n = 63 implanting blastocysts; Young -CN03 N = 5, n = 25 implanting blastocysts). Scale bar is 50μm. Two tailed p values from Mann-Whitney test. **c)** Representative images

of Aged (left) and Aged Ripasudil-treated (right) embryos fixed and stained for actin. Violin plot shows a rescue of spread area in Aged Ripasudil-treated embryos (Aged N = 4, n = 27 implanting blastocysts; Aged Ripasudil N = 3, n = 16 implanting blastocysts). Scale bar is 50μm. Two tailed p values from Mann-Whitney test.

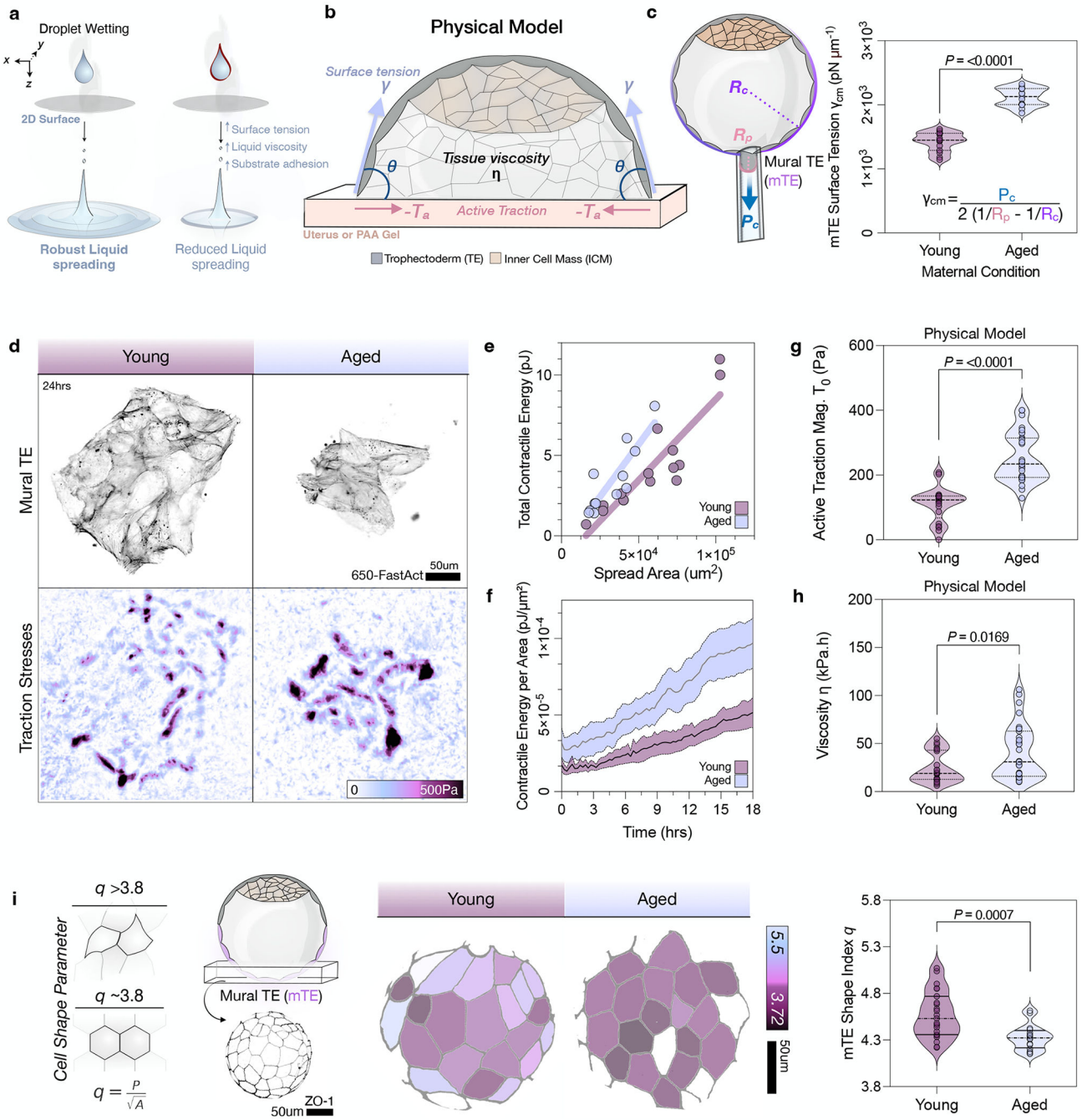

Figure 3: Advanced maternal age dampens blastocyst wetting.

a) Droplet spreading is a function of a liquid's surface tension, adhesion between the liquid and the substrate, and viscosity within the liquid. These parameters collectively determine a droplet's wetting behavior. When extrapolated to the blastocyst, key parameters dictating a tissue's spreading behavior include surface tension, cell-cell adhesion, and cell-substrate adhesion. **b)** Schematic of an implanting blastocyst as a droplet with viscosity η whose spreading is driven by active traction forces $\boldsymbol{T}_a$ and opposed by surface tension γ. The inward-pointing traction forces on the substrate ($-\boldsymbol{T}_a$) correspond to regions of cell

pulling. **c)** Schematic of Micropipette Aspiration Assay for measuring surface tension of E4.5 Blastocysts (left). The glass pipette aspirates a portion of the mural Trophectoderm region. Violin plot (right) of average surface tension measurements of E4.5 between the two maternal conditions (Young N = 3, n = 15 blastocysts; Aged N = 3, n = 15 blastocysts). Two tailed p values from Mann-Whitney test. **d)** Representative images of implanted trophectoderm stained for 650-FastAct (black) along with calculated traction stresses (purple) for both maternal conditions. Scale bar is 50 μm. **e)** Plot with each dot representing a single embryo, analyzing Total Contractile Energy (pJ) as a function of the trophectoderm's spread area (um^2) with simple linear regression to show trends. Aged embryos show higher Contractile Energy per Area compared to younger maternal controls (Young N = 3, n = 18 implanted embryos, $R^2 = 0.81$; Aged N = 3, n = 13 implanted embryos, $R^2 = 0.77$). **f)** Contractile energy per Area as calculated by Traction Force Microscopy between both maternal conditions (Young n = 18 implanted embryos; Aged n = 13 implanted embryos). Maternally aged embryos show higher strain energy per area values across the 18 hours post-implantation. Bold lines represent the mean and are bounded by shaded SEM. **g)** Plot showing Maximal Traction T_0 in both maternal conditions, as determined by fitting the physical model to the data, with higher maximal traction in the aged condition (Young n = 21 implanted embryos; Aged n = 31 implanted embryos). Two tailed p values from Mann-Whitney test. **h)** Viscosity is higher in embryos from aged mothers, as determined by fitting the physical model to the data (Young n = 21 implanted embryos; Aged n = 31 implanted embryos). Two tailed p values from Mann-Whitney test. **i)** Schematic of mTE analysis of q values (left) and representative images (right) of blastocyst cell segmentation as a function of cell shape parameter q in both maternal conditions. Aged conditions show more hexagonal cell shapes. Plot showing individual q values for cells in the mTE region of blastocysts from Young and Aged embryos (Young N = 3, n = 384 cells, 27 Blastocysts; Aged N = 3, n = 239 cells, 19 Blastocysts). Two tailed p values from Mann-Whitney test.

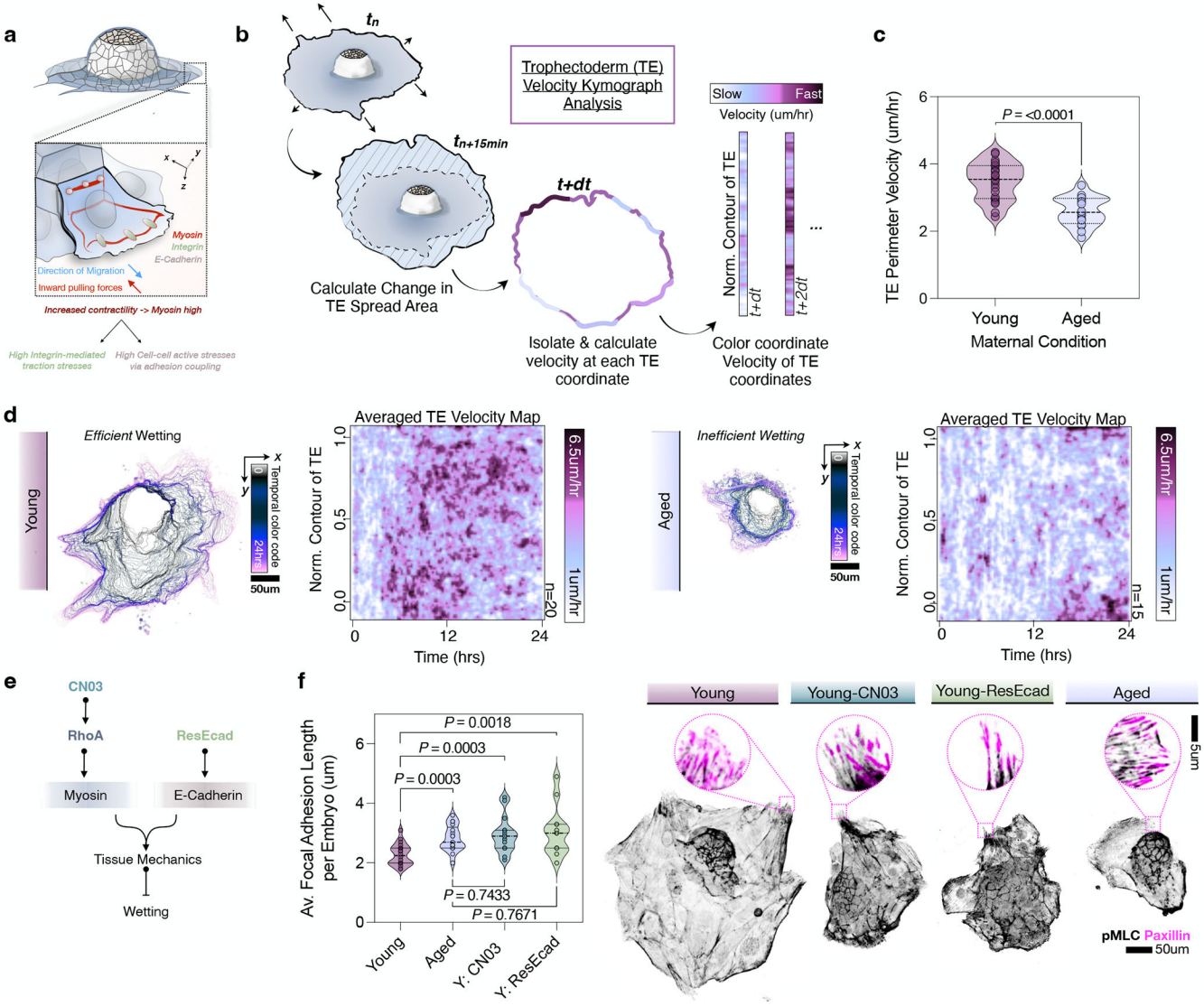

Figure 4: Embryos from aged females exhibit stronger cell-substrate focal adhesions.

a) Schematic of trophectoderm spreading in which actomyosin generates contractile forces transmitted to other cells across E-cadherin–mediated junctions and to the substrate through integrin-based adhesions. **b)** Schematic of Trophectoderm Velocity Kymograph Analysis. TE contours were segmented at successive time points, and local displacements along the perimeter were used to compute edge velocities at each coordinate. These values were mapped over time to generate velocity kymographs, enabling spatial and temporal analyses of TE spreading. **c)** Embryos from aged mothers exhibit lower Trophectoderm Perimeter Velocity. Two tailed p values from Mann-Whitney Test. **d)** Perimeter outlines and Averaged trophectoderm velocity maps for Young (left) and Aged (right) conditions. Mural Trophectoderm perimeter outlines show the evolution of trophectoderm spreading over 24 hours. Perimeter outlines are color coded based on time post-implantation. Scale bar is 50 μm. Averaged TE Velocity Maps of normalized Trophectoderm contours for Young (n=20 implanting blastocysts) and Aged (n=15 implanting blastocysts). **e)**

Schematic of pathway components contributing to tissue viscosity and reduced wetting behaviors. The cell-permeable drug CN03 activates RhoA for increased Myosin activity. Cell permeable ResEcad upregulates E-cadherin expression. Myosin-mediated forces at E-cadherin adhesions contribute to tissue viscosity and reduce tissue wetting. **f)** Quantification of Average Focal Adhesion Length per Embryo in Young (n=20 implanted embryos), Aged (n=17 implanted embryos), Young-CN03 treated (n=15 implanted embryos), and Young-ResEcad (n=12 implanted embryos) treated embryos (left). Two tailed p values from Mann-Whitney Test. Representative images of implanted embryos (right) demarcated with pMLC staining to show spread areas. Zoom images show localization of focal adhesion marker Paxillin at integrin adhesions. Scale bars are 50 μm and 5 μm, as indicated.

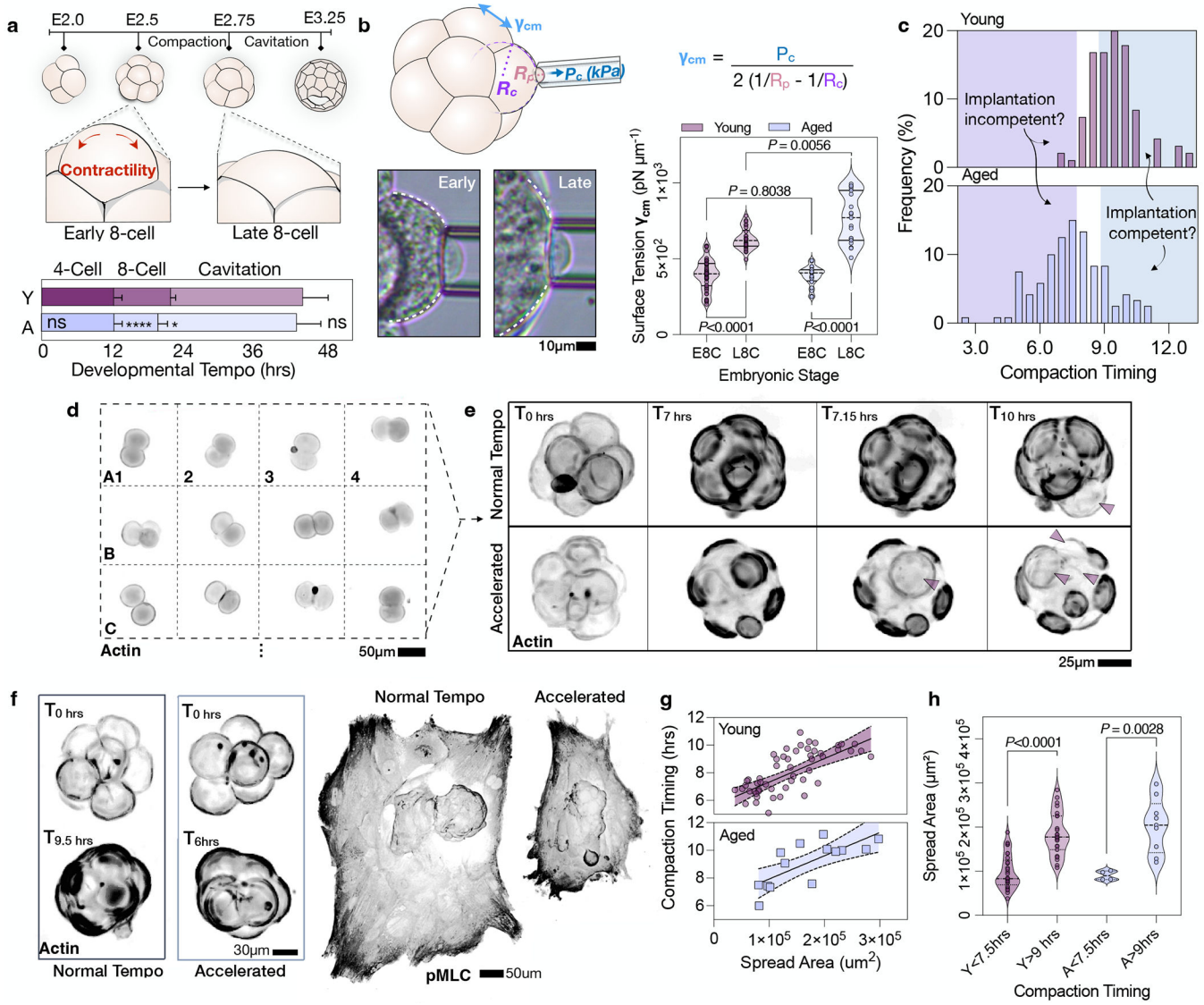

Figure 5: Compaction metrics predict implantation potential.

a) Schematic of developmental timing from the 4-cell stage through early blastocyst cavitation. At the 8-cell stage, contractility drives compaction and flattening of the embryo's outer surface. Below are the quantifications of developmental tempo for the 4-cell, 8-cell, and cavitation stages. Maternally aged embryos display a significant reduction in the timing of the 8-cell stage (N=4, Young n = 95 embryos; Aged n = 119 embryos). Error bars denote SD. Two tailed p values from Mann-Whitney test. P ns = 0.7978; ****P<0.0001; *P=0.0206 **b)** Schematic and representative images of Micropipette Aspiration Assays between early and late 8-cell stages, where the pipette aspirates the exposed apical region of the cell to calculate cortical surface tension. Analyses of cellular surface tensions show maternal age-associated increase in tension at the late 8-cell stage (Young N = 8, n = 44 Early 8-cell embryos, 26 Late 8-cell embryos; Aged N = 5, n = 24 Early 8-cell embryos, 19 Late 8-cell embryos). Two tailed p values from Mann-Whitney test. Scale bar is 10μm. **c)** Histogram of compaction tempo between both maternal conditions (N=4,

Young n = 95 embryos; Aged n = 119 embryos). Boxes highlight the expected implantation incompetent and implantation-competent windows with respect to compaction timing. **d)** Schematic of the indexing workflow for correlating compaction metrics with implantation potential. Embryos are stained for 650-FastAct and indexed at the 2-cell stage, imaged over the period of compaction, and then selected based on their developmental tempo to undergo In Vitro Implantation. Scale bar is 50μm. **e)** Representative images from timelapse imaging of embryos stained for 650-FastAct showing Normal (top) and Accelerated (bottom) compaction timing. Embryos in the Normal condition show significantly longer times to the first cell division into the 16-cell stage. Purple arrows denote cell divisions. Scale bar is 25μm. **f)** Representative images of embryos live-imaged at the 8-cell stages (black, 650-FastAct) undergoing compaction (left) and their representative fixed, implanted embryos (black, pMLC staining) (right). Scale bars are 30μm and 50μm, as indicated. **g)** Plot of compaction timing as a function of final Trophectoderm spread area 48 hours post-implantation for both maternal conditions (N=3, Young n = 56 implanted blastocysts; N=2, Aged n = 14 implanted blastocysts). Bold line represents simple linear regression and are bounded by 95% Confidence Interval (Young $R^2 = 0.40$; Aged $R^2 = 0.55$). **h)** Violin plots from (f) show spread area binned by their compaction timing of either >9hrs or <7.5hrs. Both Young and aged conditions show significant reductions in spread area if their compaction timing falls within the <7.5hrs compaction category (N = 3: Young n = 23 >9hrs, 29 <7.5hrs; N = 2: Aged n = 9 >9hrs, 5 <7.5hrs). Two tailed p values from Mann-Whitney test.

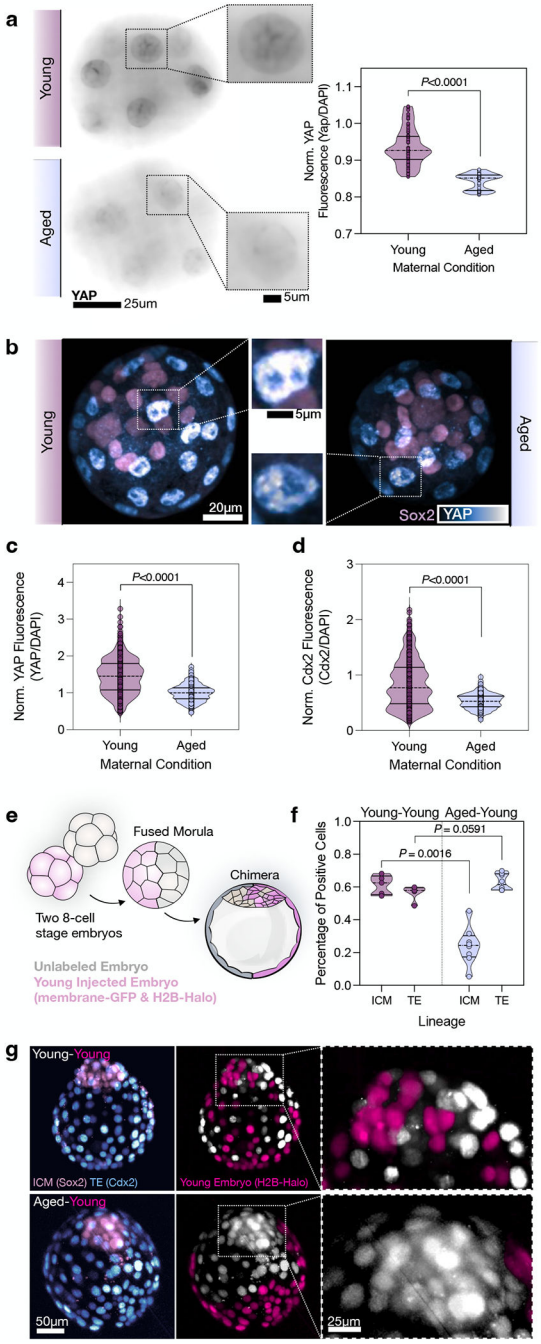

Figure 6: Embryos from aged females display trophectoderm-specific cell fate defects.

a) (Left) Representative images of summed intensity projections of YAP staining in Young and Aged 8-cell embryos. Scale bar are 25 µm and 5 µm, as indicated. (Right) Quantification of normalized YAP fluorescence intensities in Young (n=59 cells, 8 embryos) and Aged (n=37 cells, 7 embryos) maternal conditions show an age-related reduction in nuclear YAP intensity. Two tailed p values from Mann-Whitney Test. **b)** Representative images of E3.5 blastocysts from Young and Aged conditions. The Inner Cell Mass (purple) is marked by Sox2 expression, and Trophectoderm (cyan) is marked by YAP expression. Scale bars are

20 μm and 5 μm, as indicated. **c)** Quantification of normalized YAP fluorescence intensities in Young (n=27 blastocysts) and Aged (n=37 blastocysts) show age-associated reduction in nuclear YAP expression. Two tailed p values from Mann-Whitney Test. **d)** Quantification of normalized Cdx2 fluorescence intensities in Young (n=27 blastocysts) and Aged (n=37 blastocysts) show age-associated reduction in nuclear Cdx2 expression, indicating a depletion of the Trophectoderm lineage. Two tailed p values from Mann-Whitney Test. **e)** Schematic of chimera generation in which we test how the mechanics of young vs aged embryos impacts cell position and cell fate. Two 8-cell stage embryos are placed in contact with one other, enabling their fusion into a chimeric morula that undergoes cavitation to blastocyst formation. **f)** Percentage of H2B-positive cells from injected and labeled Young embryos within the chimeric lineages. In the Young-Young chimera (n=5 chimeras), H2B labeled Young embryonic cells contribute heavily to both trophectoderm and inner cell mass lineages. In the Aged-Young Chimera (n=8 chimeras), there is a reduction in the number of H2B-positive Young embryonic cells in the Inner Cell Mass, reflecting a chimera in which the Aged unlabeled embryo preferentially contributes to this lineage. Two tailed p values from Mann-Whitney Test. **g)** Representative images of heterochronic chimeras. Young-Young chimeras show a mixing of H2B-labeled Young embryonic cells (magenta) to the Inner Cell Mass (Sox2 positive, purple) and Trophectoderm (Cdx2 positive, cyan). Aged-Young chimeras show a lack of mixing between the two contributing embryos, with the majority of the Inner Cell Mass arising from the Aged unlabeled embryo. The propensity of cells from aged embryos to contribute to the ICM vs Trophectoderm could explain the depletion of Trophectoderm cells in aged embryos. Scale bars are 50 μm and 25 μm as indicated.

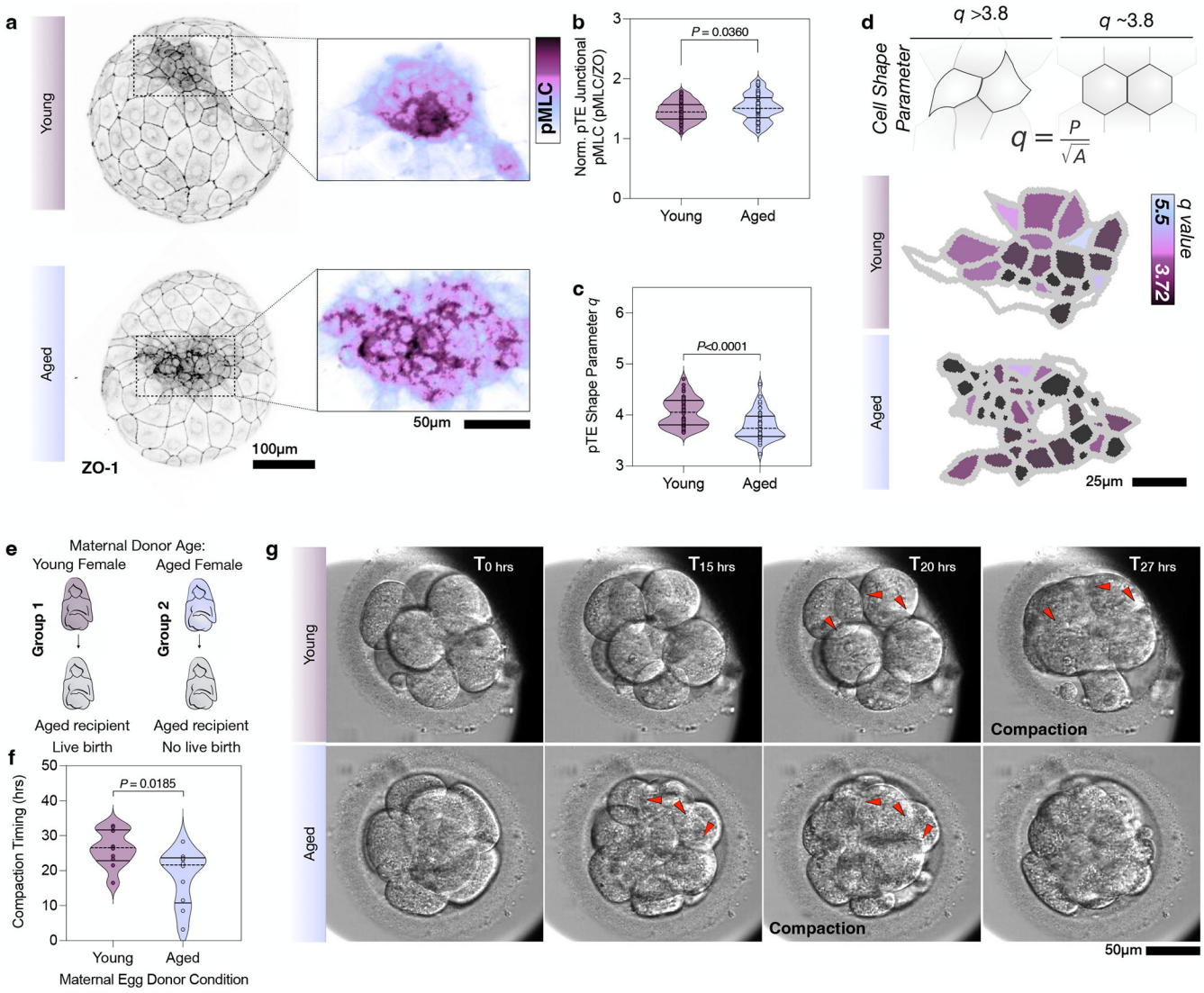

Figure 7: Human embryos from older women display heightened contractility.

a) Representative immunofluorescence z-projection image of Young (top) and Aged (bottom) human blastocyst stained for junctional marker ZO-1 (black, left). Inlays (right) show sum intensity projections of pMLC staining (purple) of the polar trophectoderm in Young (top) and Aged (bottom) blastocysts. Scale bar is 100μm and 50μm, where indicated. **b)** Quantifications of normalized junctional pMLC in the future human implantation site (polar trophectoderm) region displayed in (A). Young embryos (n = 179 junctions, 2 blastocysts) show lower normalized pTE junctional pMLC than Aged embryos (n = 111 junctions, 1 blastocyst). Two tailed p values from Welch's t test. **c)** Quantifications of cell shape parameter q in polar trophectoderm region of human blastocysts displayed in (A). Aged blastocyst shows decreases in shape parameter compared to Young blastocysts. Two tailed p values from Mann-Whitney test. **d)** Schematic of cell shape parameter quantification (top) with representative images of blastocyst's polar trophectoderm cells color coded by their shape parameter. Lighter values depict more irregular shapes and darker purple values show lower q values and more hexagonal shapes. Scale bar is 25μm. **e)** Schematic of age

groups selected for Embryoscope analysis from IVF datasets. Group 1 contains embryos donated from women <28 years and transferred to aged recipients, after which a live birth was recorded. Group 2 contains euploid embryos donated from women >40 years and transferred to aged recipients, after which no live birth was recorded. **f)** Quantification of compaction timing for Young (n = 10 embryos) and Aged (n = 10 embryos) shows Aged embryos have significantly faster timing to initial compaction. Two tailed p values from Mann-Whitney test. **g)** Representative images of Young embryo (top) and Aged embryo (bottom) undergoing compaction. Red arrows indicate transition from optically visible junctions to disappearing junctions post-compaction. Scale bar is 50μm.

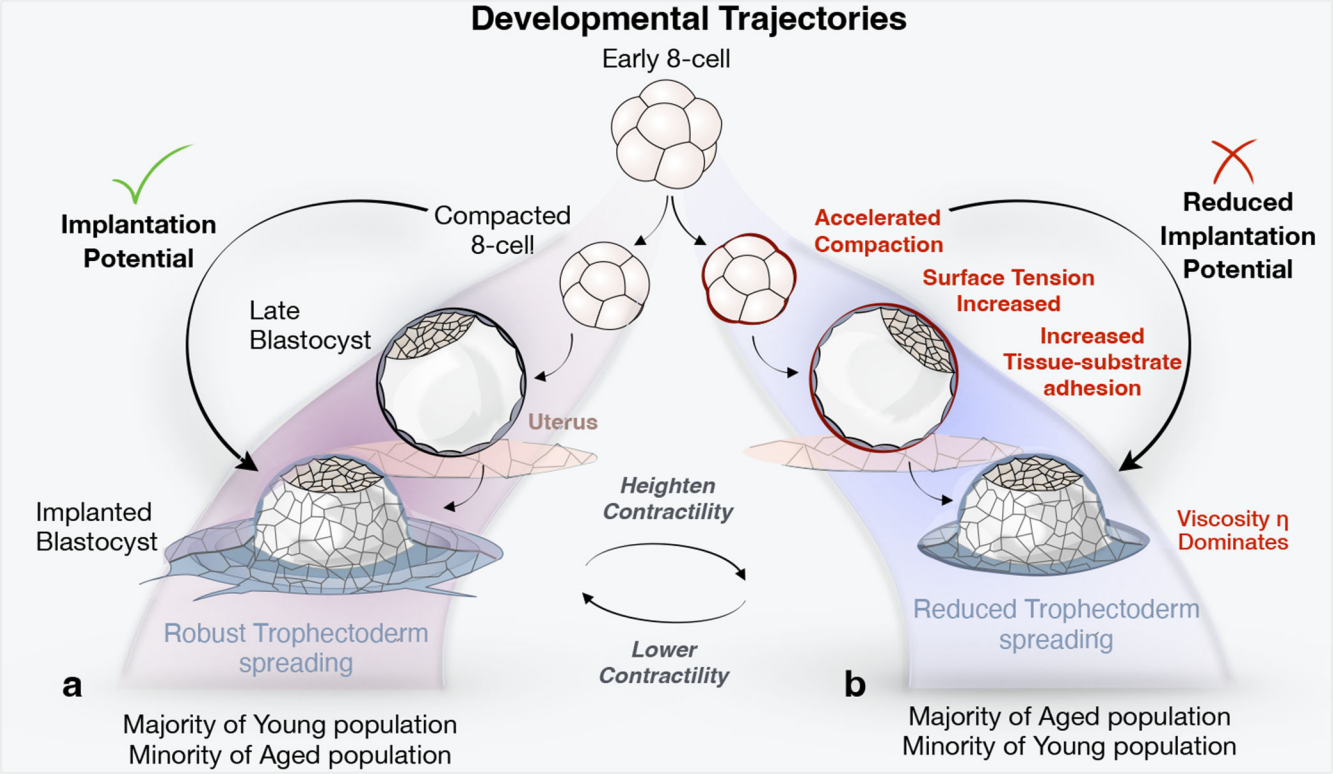

Figure 8: Summary Figure. Contractility shifts the proportion of implantation-competent embryos in the Young and Aged maternal condition.

a) Schematic of developmental trajectory in the embryos that are competent to implant. Compaction proceeds normally at ~ 9 h, followed by blastocyst formation and implantation to yield robust trophectoderm spreading. During wetting in these embryos, tissue-substrate adhesion forces dominate to produce robust trophectoderm spreading. The majority of Young embryos and minority of Aged embryos display this spreading behavior. Embryos that are incompetent to implant can be shifted to exhibit efficient wetting through lowering contractility. **b)** Schematic of developmental trajectory in the embryos that are incompetent to implant. Compaction is accelerated on average 2 hours faster due to aberrant contractility, that acts to increase surface tension at the blastocyst stage and impair trophectoderm fate specification. Upon substrate adhesion, tissue viscosity dominates to reduce wetting and slow trophectoderm spreading and implantation. The majority of Aged embryos and minority of Young embryos display this spreading deficiency. This spreading defect can be phenocopied in implantation-competent embryos by increasing contractile activity.